



Diving Beneath the Sea of Stellar Activity: Chromatic Radial Velocities of the Young AU Mic Planetary System

Bryson L. Cale¹, Michael Reefe¹, Peter Plavchan¹, Angelle Tanner², Eric Gaidos³, Jonathan Gagné^{4,5}, Peter Gao⁶, Stephen R. Kane⁷, Víctor J. S. Béjar^{8,9}, Nicolas Lodieu^{8,9}, Guillem Anglada-Escudé^{10,11}, Ignasi Ribas^{10,11}, Enric Palle^{8,9}, Andreas Quirrenbach¹², Pedro J. Amado¹³, Ansgar Reiners¹⁴, José A. Caballero¹⁵, María Rosa Zapatero Osorio¹⁶, Stefan Dreizler¹⁴, Andrew W. Howard¹⁷, Benjamin J. Fulton¹⁸, Sharon Xuesong Wang¹⁹, Kevin I. Collins¹, Mohammed El Mufti¹, Justin Wittrock¹, Emily A. Gilbert^{20,21,22,23,24}, Thomas Barclay^{25,26}, Baptiste Klein²⁷, Eder Martioli^{28,29}, Robert Wittenmyer³⁰, Duncan Wright³⁰, Brett Addison³⁰, Teruyuki Hirano^{31,32,33}, Motohide Tamura^{31,32,34}, Takayuki Kotani^{31,32,33}, Norio Narita^{31,35,36,37}, David Vermilion¹, Rena A. Lee³⁸, Claire Geneser², Johanna Teske³⁹, Samuel N. Quinn⁴⁰, David W. Latham⁴⁰, Gilbert A. Esquerdo⁴⁰, Michael L. Calkins⁴⁰, Perry Berlind⁴⁰, Farzaneh Zohrabi⁴¹, Caitlin Stibbards¹, Srihan Kotnana^{1,42}, Jon Jenkins⁴³, Joseph D. Twicken^{43,44}, Christopher Henze⁴³, Richard Kidwell, Jr.⁴⁵, Christopher Burke⁴⁶, Joel Villaseñor⁴⁶, and Patricia Boyd⁴⁷

¹ George Mason University, 4400 University Drive, Fairfax, VA 22030, USA; bryson.cale1@gmail.com

² Mississippi State University, 75 B. S. Hood Road, Mississippi State, MS 39762, USA

³ University of Hawai'i at Manoa, 1680 East-West Road, Honolulu, HI 96822, USA

⁴ Planétarium Rio Tinto Alcan, Espace pour la vie, 4801 av. Pierre-De Coubertin, Montréal, QC H1V 3V4, Canada

⁵ Institute for Research on Exoplanets, Université de Montréal, Département de Physique, C.P. 6128 Succ. Centre-ville, Montréal, QC H3C 3J7, Canada

⁶ University of California, Santa Cruz, 1156 High Street, Santa Cruz, CA 95064, USA

⁷ University of California, Riverside, 900 University Avenue Riverside, CA 92521, USA

⁸ Instituto de Astrofísica de Canarias, E-38205 La Laguna, Tenerife, Spain

⁹ Departamento de Astrofísica, Universidad de La Laguna, E-38206 La Laguna, Tenerife, Spain

¹⁰ Institut de Ciències de l'Espai (ICE, CSIC), Campus UAB, Can Magrans s/n, E-08193 Bellaterra, Spain

¹¹ Institut d'Estudis Espacials de Catalunya (IEEC), E-08034 Barcelona, Spain

¹² Landessternwarte, Zentrum für Astronomie der Universität Heidelberg, Königstuhl 12, D-69117 Heidelberg, Germany

¹³ Instituto de Astrofísica de Andalucía (CSIC), Glorieta de la Astronomía s/n, E-18008 Granada, Spain

¹⁴ Institut für Astrophysik, Georg-August-Universität, Friedrich-Hund-Platz 1, D-37077 Göttingen, Germany

¹⁵ Centro de Astrobiología (CSIC-INTA), ESAC, Camino bajo del castillo s/n, E-28692 Villanueva de la Cañada, Madrid, Spain

¹⁶ Centro de Astrobiología (CSIC-INTA), Carretera de Ajalvir km 4, E-28850 Torrejón de Ardoz, Madrid, Spain

¹⁷ California Institute of Technology, 1200 E California Blvd, Pasadena, CA 91125, USA

¹⁸ IPAC, 770 South Wilson Avenue, Pasadena, CA 91125, USA

¹⁹ Department of Astronomy, Tsinghua University, Beijing 100084, People's Republic of China

²⁰ Department of Astronomy and Astrophysics, University of Chicago, 5640 S. Ellis Avenue, Chicago, IL 60637, USA

²¹ University of Maryland, Baltimore County, 1000 Hilltop Circle, Baltimore, MD 21250, USA

²² The Adler Planetarium, 1300 South Lakeshore Drive, Chicago, IL 60605, USA

²³ NASA Goddard Space Flight Center, 8800 Greenbelt Road, Greenbelt, MD 20771, USA

²⁴ NASA Goddard Space Flight Center Sellers Exoplanet Environments Collaboration, 8800 Greenbelt Road, Greenbelt, MD 20771, USA

²⁵ NASA Goddard Space Flight Center, 800 Greenbelt Road, Greenbelt, MD 20771, USA

²⁶ University of Maryland Baltimore County, 1000 Hilltop Circle, Baltimore, MD 21250, USA

²⁷ Sub-department of Astrophysics, Department of Physics, University of Oxford, Oxford OX1 3RH, UK

²⁸ Institut d'Astrophysique de Paris, CNRS, UMR 7095, Sorbonne Université, 98 bis bd Arago, F-75014 Paris, France

²⁹ Laboratório Nacional de Astrofísica, Rua Estados Unidos 154, Itajubá, MG 37504-364, Brazil

³⁰ University of Southern Queensland, West St, Darling Heights, QLD 4350, Australia

³¹ Astrobiology Center, 2-21-1 Osawa, Mitaka, Tokyo 181-8588, Japan

³² National Astronomical Observatory of Japan, NINS, 2-21-1 Osawa, Mitaka, Tokyo 181-8588, Japan

³³ Department of Astronomical Science, School of Physical Sciences, The Graduate University for Advanced Studies (SOKENDAI), 2-21-1, Osawa, Mitaka, Tokyo, 181-8588, Japan

³⁴ Department of Astronomy, Graduate School of Science, The University of Tokyo, 7-3-1 Hongo, Bunkyo-ku, Tokyo 113-0033, Japan

³⁵ Komaba Institute for Science, The University of Tokyo, 3-8-1 Komaba, Meguro, Tokyo 153-8902, Japan

³⁶ JST, PRESTO, 3-8-1 Komaba, Meguro, Tokyo 153-8902, Japan

³⁷ Instituto de Astrofísica de Canarias (IAC), E-38205 La Laguna, Tenerife, Spain

³⁸ University of Hawai'i at Manoa, 2500 Campus Road, Honolulu, HI 96822, USA

³⁹ Carnegie Earth and Planets Laboratory, 5241 Broad Branch Road, N.W., Washington, DC 20015-1305, USA

⁴⁰ Center for Astrophysics, Harvard and Smithsonian, 60 Garden Street, Cambridge, MA 02138, USA

⁴¹ Louisiana State University, 202 Nicholson Hall, Baton Rouge, LA 70803, USA

⁴² Westfield High School, 4700 Stonecroft Blvd, Chantilly, VA 20151, USA

⁴³ NASA Ames Research Center, Moffett Field, CA 94035, USA

⁴⁴ SETI Institute, Mountain View, CA 94043, USA

⁴⁵ Mikulski Archive for Space Telescopes, 3700 San Martin Drive, Baltimore, MD 21218, USA

⁴⁶ Department of Physics and Kavli Institute for Astrophysics and Space Research Massachusetts Institute of Technology, 70 Vassar Street, Cambridge, MA 02139, USA

⁴⁷ Astrophysics Science Division, NASA Goddard Space Flight Center, 800 Greenbelt Road, Greenbelt, MD 20771, USA

Received 2021 July 1; revised 2021 September 14; accepted 2021 October 1; published 2021 December 7

Abstract

We present updated radial-velocity (RV) analyses of the AU Mic system. AU Mic is a young (22 Myr) early-M dwarf known to host two transiting planets— $P_b \sim 8.46$ days, $R_b = 4.38^{+0.18}_{-0.18} R_{\oplus}$, $P_c \sim 18.86$ days, $R_c = 3.51^{+0.16}_{-0.16} R_{\oplus}$. With visible RVs from Calar Alto high-Resolution search for M dwarfs with ExoEarths with Near-infrared and optical

echelle Spectrographs (CARMENES)-VIS, CHIRON, HARPS, HIRES, MINERVA-Australis, and Tillinghast Reflector Echelle Spectrograph, as well as near-infrared (NIR) RVs from CARMENES-NIR, CSHELL, IRD, iSHELL, NIRSPEC, and SPIRou, we provide a 5σ upper limit to the mass of AU Mic c of $M_c \leq 20.13 M_\oplus$ and present a refined mass of AU Mic b of $M_b = 20.12^{+1.72}_{-1.57} M_\oplus$. Used in our analyses is a new RV modeling toolkit to exploit the wavelength dependence of stellar activity present in our RVs via wavelength-dependent Gaussian processes. By obtaining near-simultaneous visible and near-infrared RVs, we also compute the temporal evolution of RV “color” and introduce a regressional method to aid in isolating Keplerian from stellar activity signals when modeling RVs in future works. Using a multiwavelength Gaussian process model, we demonstrate the ability to recover injected planets at 5σ significance with semi-amplitudes down to $\approx 10 \text{ m s}^{-1}$ with a known ephemeris, more than an order of magnitude below the stellar activity amplitude. However, we find that the accuracy of the recovered semi-amplitudes is $\sim 50\%$ for such signals with our model.

Unified Astronomy Thesaurus concepts: Exoplanets (498)

1. Introduction

Characterizing young planetary systems is key to improving our understanding of their formation and evolution. Young transiting systems in particular offer a means to directly probe the radii, and together with masses from precise radial-velocity (RV) measurements, the bulk densities of the planets. RV observations are also crucial to constrain the eccentricity of the orbit to understand the kinematic history and stability of the system. A precision of 20% for the mass determination is further recommended for enabling detailed atmospheric characterization, particularly for terrestrial-mass planets (Batalha et al. 2019).

Unfortunately, searches for planets orbiting young stars have been limited by stellar activity signals comparable in amplitude to that of typical Keplerian signals. Stellar surface inhomogeneities (e.g., cool spots, hot plages) driven by the dynamic stellar magnetic field rotate in and out of view, leading to photometric variations over time. The presence of such active regions breaks the symmetry between the approaching and receding limbs of the star, introducing RV variations over time as well (Desort et al. 2007). These active regions further affect the integrated convective blueshift over the stellar disk, and will therefore manifest as an additional net red- or blueshift (Meunier & Lagrange 2013; Dumusque et al. 2014). Various techniques have been introduced to lift the degeneracy between activity- and planetary-induced signals in RV data sets, such as line-by-line analyses (Dumusque 2018; Wise et al. 2018; Cretignier et al. 2020) and Gaussian process (GP) modeling (e.g., Haywood et al. 2014; Grunblatt et al. 2015; López-Morales et al. 2016; Plavchan et al. 2020; Robertson et al. 2020; Klein et al. 2021; Toledo-Padrón et al. 2021), but such measurements remain challenging due to the sparse cadence of typical RV data sets compared to the activity timescales.

AU Mic is a young (22 Myr; Mamajek & Bell 2014), nearby (β Pictoris moving group, ~ 10 pc; Gaia Collaboration et al. 2018), and active pre-main-sequence M1 dwarf (Plavchan et al. 2020, hereafter referred to as P20). AU Mic hosts an edge-on debris disk (Pecaut & Mamajek 2013), and therefore the probability for planets to transit is greater than for other systems. Using photometric observations from TESS (Ricker et al. 2015) in Sector 1 (2018 July 25–August 22), P20 discovered an ≈ 8.46 day Neptune-size ($R_b = 4.38^{+0.18}_{-0.18} R_\oplus$) transiting planet, which was further validated to transit with Spitzer observations (hereafter referred to as AU Mic b). P20 also reported the detection of a single-transit event in the TESS Sector 1 light curve, but did not constrain the period with only an isolated event. With high-cadence RVs from SPIRou, Klein et al. (2021; hereafter referred to as K21) measured the mass of AU Mic b and confirmed it to be consistent with a Neptune-

mass planet ($M_b = 17.1^{+4.7}_{-4.5} M_\oplus$). With more observations of AU Mic from the TESS extended mission in Sector 27 (2020 July 4–30), Martioli et al. (2021; hereafter referred to as M21) determined AU Mic c to be a smaller Neptune-sized planet ($R_c = 3.51^{+0.16}_{-0.16} R_\oplus$) with a period of ≈ 18.86 days.

In this paper, we present and discuss analyses of several years of multiwavelength RV observations of AU Mic that further elucidates this planetary system. In Section 2, we summarize the visible and near-infrared (NIR) RV observations, as well as photometric observations that are used to inform our RV model. In Section 3, we introduce two joint quasi-periodic Gaussian process kernels that are initial steps in taking into account the expected wavelength dependence of stellar activity through simple scaling relations between wavelengths. We then apply our model to RVs of AU Mic and present the results in Section 4. In Section 5, we assess the sensitivity of our RV model through planet injection and recovery tests. We then briefly discuss the utility of “RV color” between two wavelengths in isolating Keplerian from stellar-activity-induced signals in Section 5.4. We finally note the assumptions and caveats in this work in Section 5.5. A summary of this work is provided in Section 6.

2. Observations

2.1. RVs

Our analyses make use of new and archival high-resolution echelle spectra from a variety of facilities, which are summarized in Table 1. We briefly detail new spectroscopic observations and the corresponding RVs from observing programs primarily intended to characterize the AU Mic planetary system.

2.1.1. CARMENES

The Calar Alto high-Resolution search for M dwarfs with Exoearths with Near-infrared and optical echelle Spectrographs (CARMENES) instrument (Quirrenbach et al. 2018) is a pair of two high-resolution spectrographs installed at the 3.5 m telescope at the Calar Alto Observatory in Spain. The visual (VIS) and near-infrared (NIR) arms cover a wavelength range of 520–960 nm and 960–1710 nm, with resolving powers of $R = 94,600$ and $R = 80,400$, respectively. AU Mic was observed 100 times with CARMENES during two different campaigns between 2019 July 14 and October 9, and between 2020 July 19 and November 16, respectively. This last observing period was partially contemporaneous with TESS observations of AU Mic in Sector 27 (2020 July 4–30). One or two exposures of 295 s were obtained per epoch with typical signal-to-noise ratio (S/N) larger than 70–100, and at airmasses larger than 2.5, due to the low decl. of the target at the

Table 1
A Summary of the RV Data Sets Used in This Work

Spectrograph/Facility	$\lambda/\Delta\lambda [\times 10^3]$	N_{nights}	N_{used}	Median σ_{RV} (m s $^{-1}$)	Adopted λ (nm)	Pipeline	Comm. Paper
HIRES/Keck	85	60	41	2.6	565	...	Vogt et al. (1994)
Tillinghast/TRES	44	85	55	24.2	650	...	Fűrész (2008)
CARMENES-VIS/Calar Alto 3.5 m	94.6	63	60	11.4	750	caracal (Caballero et al. 2016) serval (Zechmeister et al. 2018)	Bauer et al. (2020)
CARMENES-NIR/Calar Alto 3.5 m	80.4	62	49	32.6	1350
SPIRou/CFHT	75	27	27	5.0	1650	K21	Donati et al. (2018)
iSHELL/IRTF	85	46	31	5.0	2350	pychell Cale et al. (2019)	Rayner et al. (2016)
HARPS-S/La Silla 3.6 m	115	34	0	2.2	565	ESO DRS (Lo Curto et al. 2010) HARPS-TERRA (Anglada-Escudé & Butler 2012)	Mayor et al. (2003)
MINERVA- Australis-T3	80	13	0	9.5	565	(Anglada-Escudé & Butler 2012)	Wittenmyer et al. (2018), Addison et al. (2019, 2021)
MINERVA- Australis-T4	80	13	0	9.5	565
MINERVA- Australis-T6	80	13	0	9.5	565
CHIRON/CTIO	136	12	0	46	565	Piskunov & Valenti (2002), Cale et al. (2019)	Tokovinin et al. (2013)
IRD/Subaru	70	6	0	3.0	1350	IRAF; (Tody 1993) Hirano et al. (2020b)	Kotani et al. (2018)
NIRSPEC/Keck	25	14	0	50	2350	Bailey et al. (2012)	McLean et al. (1998)
CSHELL/IRTF	36	21	0	26	2350	Gagné et al. (2016), Gao et al. (2016)	Greene et al. (1993)

Note. The nightly binned measurements are provided in Appendix C. N_{tot} and N_{nights} refer to the numbers of individual and per-night epochs, respectively. The median intrinsic error bars σ_{RV} consider all observations. All RV measurements are provided in Table 7.

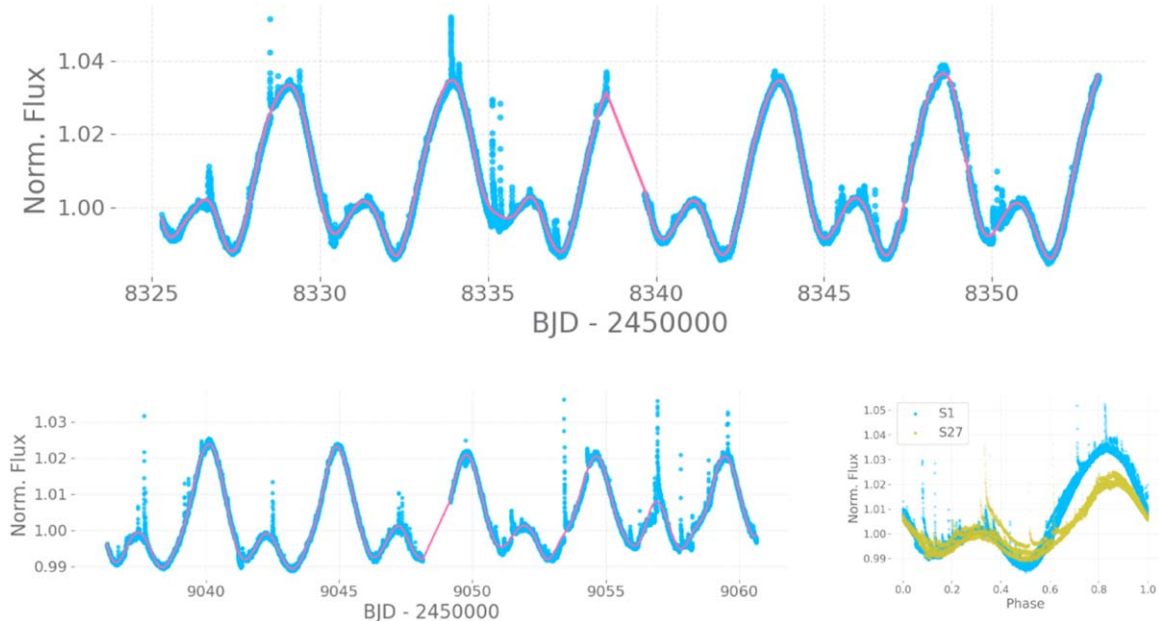


Figure 1. The TESS PDCSAP light curves of AU Mic from Sectors 1 (top) and 27 (bottom). The lower right plot shows both sectors phased to 4.836 days. Although the two seasons exhibit nearly identical periodic signals, Sector 27 exhibits moderate evolution. The least-squares cubic spline fit for each sector is shown in pink.

Calar Alto observatory. CARMENES data were processed by the *caracal* pipeline (Caballero et al. 2016), which includes bias, flat-field, and dark correction, tracing the echelle orders on the detector, optimal extraction of the one-dimensional spectra, and performance of the initial wavelength calibration using U-Ar, U-Ne, and Th-Ne lamps. The RVs were obtained with the *serval* pipeline (Zechmeister et al. 2018) by cross-correlating the observed spectrum with a reference template constructed from all observed spectra of the same star. In addition, the *serval* pipeline also computes the correction for barycentric motion, secular acceleration, instrumental drift using simultaneous observations of Fabry-Pérot etalons, and nightly zero points using RV standards observed during the night (Trifonov et al. 2018).

2.1.2. CHIRON

We obtained 14 nightly observations of AU Mic with the CHIRON spectrometer (Kotani et al. 2018) on the SMARTS 1.5 m telescope at the Cerro Tololo Inter-American Observatory (CTIO) between UT dates 2019 September 14 and November 10. Observations are recorded in narrow slit mode ($R \sim 136,000$) using the iodine cell to simultaneously calibrate for the wavelength scale and instrument profile. Like iSHELL observations (see Cale et al. 2019), exposure times (t_{exp}) were limited to 5 minutes due to the uncertainties of barycenter corrections scaling as t_{exp}^2 (Tronsgaard et al. 2019), and the dynamicity of telluric absorption over a single exposure. We initially recorded 22 exposures per night, and later increased this to 42 because the cumulative S/N within a night was insufficient (~ 100).⁴⁸ Raw CHIRON observations are reduced via the REDUCE package

(Piskunov & Valenti 2002), and the corresponding RVs are computed using *pychell*. Unfortunately, a significant fraction of the extracted one-dimensional spectra are too noisy to robustly measure the precise RVs from (peak S/N ≈ 20 –30 per spectral pixel). We therefore flag clear outliers in the RV measurements, and recompute the nightly (binned) RVs, resulting in 12 epochs to be included in our analyses.

2.1.3. HIRES

We include 60 Keck-HIRES (Vogt et al. 1994) observations of AU Mic in our analyses. The majority of these observations took place in the second half of 2020, with several nights yielding contemporaneous observations with other facilities. Exposure times range from 204 to 500 s, yielding a median S/N ≈ 234 at 550 nm per spectral pixel. HIRES spectra are processed and RVs computed via methods described in Howard et al. (2010).

2.1.4. MINERVA-Australis

Spectroscopic observations of AU Mic were carried out using the MINERVA-Australis facility situated at the Mount Kent Observatory in Queensland, Australia (Wittenmyer et al. 2018; Addison et al. 2019, 2021) between 2019 July 18 and November 5. MINERVA-Australis consists of an array of four independently operated 0.7 m CDK700 telescopes, three of which were used in observing AU Mic. Each telescope simultaneously feeds stellar light via fiber optic cables to a single KiwiSpec R4-100 high-resolution ($R \sim 80,000$) spectrograph (Barnes et al. 2012) with wavelength coverage from 480 to 620 nm. In total, we obtained 31 observations with telescope 3 (M-A Tel3), 35 observations with telescope 4 (M-A Tel4), and 33 observations with telescope 6 (M-A Tel6). Exposure times for these observations were set to 1800 s, providing an S/N between 15 and 35 per spectral pixel. RVs are derived for each telescope by using the least-squares shift and fit technique (Anglada-Escudé & Butler 2012), where the template being matched is the mean spectrum of each

⁴⁸ Unlike iSHELL (and like many modern echelle spectrographs), CHIRON makes use of an exposure meter in order to calculate the proper (flux-weighted) exposure midpoint, and therefore longer exposure times will be impacted less by the uncertainty in computing the exposure midpoint. Further, tellurics at visible wavelengths are far more sparse than for iSHELL at *K*-band wavelengths. We therefore recommend significantly longer exposure times (≥ 30 minutes) for future observations of AU Mic (or targets of similar brightness) with CHIRON in narrow slit mode.

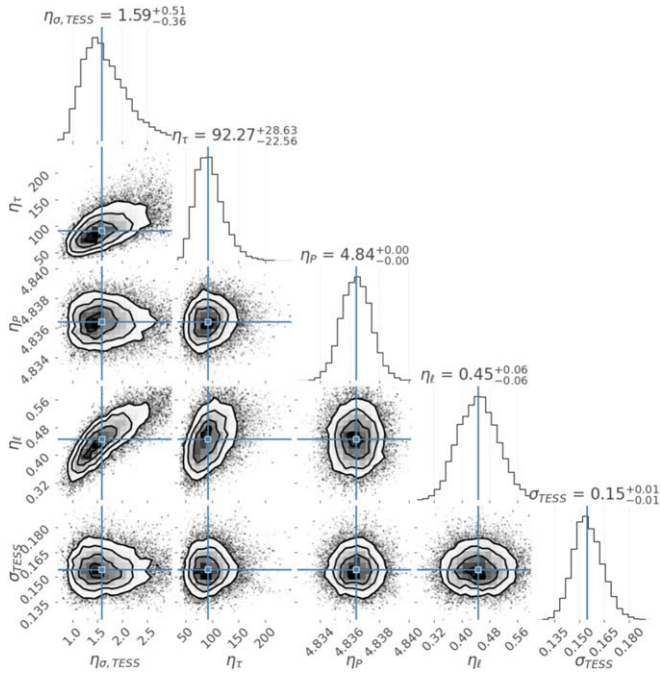


Figure 2. Posterior distributions from fits to the predicted RV variability from the FF' technique (Equation (5)).

telescope. Spectrograph drifts are corrected for using simultaneous thorium–argon (ThAr) arc lamp observations.

2.1.5. TRES

We include 85 observations (archival and new) of AU Mic observed with the Tillinghast Reflector Echelle Spectrograph (TRES; Fűrész 2008) in our analyses. The majority of these observations took place in the second half of 2019, with several nights yielding contemporaneous observations with other facilities. Typical exposure times range from 600 to 1200 s, with a median $S/N \approx 60$ per resolution element. Spectra are processed using methods outlined in Buchhave et al. (2010) and Quinn et al. (2014), with the exception of the cross-correlation template, for which we use the high-S/N median observed spectrum.

2.1.6. IRD

We obtained near-infrared, high-resolution spectra of AU Mic using the InfraRed Doppler (IRD) instrument (e.g., Kotani et al. 2018) on the Subaru 8.2 m telescope. The observations were carried out between 2019 June and October, and we obtained a total of 430 frames with integration times of 30–60 s. Half of these frames were taken on the transit night (UT 2019 June 17), with the goal of measuring the stellar obliquity for AU Mic b, whose RVs were already presented in Hirano et al. (2020a). The raw data are reduced in a standard manner using our custom code as well as `IRAF` (Tody 1993), and the extracted one-dimensional spectra are analyzed by the RV-analysis pipeline for IRD as described in Hirano et al. (2020b). The typical precision of the derived RVs is $9\text{--}13\text{ m s}^{-1}$.

2.1.7. iSHELL

We obtained 46 out-of-transit observations of AU Mic with iSHELL on the NASA Infrared Telescope Facility (Rayner et al. 2016) from 2016 to 2020 October. The exposure times

varied from 20 to 300 s, and the exposures were repeated 2–23 times within a night to reach a cumulative S/N per spectral pixel >200 (the approximate center of the blaze for the middle order, $2.35\text{ }\mu\text{m}$) for most nights. Raw iSHELL spectra are processed in `pychell` using methods outlined in Cale et al. (2019).

The corresponding iSHELL RVs are computed in `pychell` using updated methods to those described in Cale et al. (2019). Instead of starting from an unknown (flat) stellar template, we start with a BT-Settl (Allard et al. 2012) stellar template with $T_{\text{eff}} = 3700\text{ K}$, and with solar values for $\log g$ and Fe/H . We further Doppler-broaden the template using the `rotBroad` routine from PyAstronomy (Czesla et al. 2019) with $v \sin i = 8.8\text{ km s}^{-1}$. Qualitatively, this broadened template matches the iSHELL observations well. We also “iterate” the template by co-adding residuals in a quasi-inertial reference frame with respect to the star according to the barycenter velocities (v_{BC}). However, the stellar RVs for subsequent iterations tend to be highly correlated with v_{BC} and exhibit significantly larger scatter than the first iteration suggests. We therefore use RVs from the first iteration only, and leave the cause of this correlation as a subject for future work.

2.2. Photometry from TESS

The NASA TESS mission (Ricker et al. 2015) observed AU Mic in Sectors 1 (2018 July 25–August 22) and 27 (2020 July 4–30). We download the light curves from the Mikulski Archive for Space Telescopes (MAST; Swade et al. 2018). We use the Science Processing Operations Center (SPOC; Jenkins et al. 2016) “Presearch Data Conditioning” light curves utilizing “Simple Aperture Photometry” (PDCSAP; Smith et al. 2012; Stumpe et al. 2012, 2014) to inform our model in Section 3.3.1.

3. Radial-velocity Fitting

3.1. Bayesian Inference for Radial Velocities

We primarily seek to utilize a global (joint) Gaussian process model with multiple realizations that give rise to the data we observe with all of the above instruments simultaneously. To implement our desired framework, we have developed two `Python` packages. We leave the description of `optimize`—a high-level Bayesian inference framework to Appendix B.

To provide RV-specific routines, we extend the `optimize` package within the `orbits` submodule of the `pychell` (Cale et al. 2019) package.⁴⁹ We define classes specific for RV data, models, and likelihoods, with much of the “boilerplate” code handled through `optimize`. A top-level “RVProblem” further defines a pool of RV-specific methods for pre- and post-optimization routines, such as plotting phased RVs, periodogram tools, model comparison tests, and propagation of Markov-Chain Monte Carlo (MCMC) chains for deterministic Keplerian parameters (e.g., planet masses, semimajor axes, and densities).

3.2. Two Chromatic Gaussian Processes

A Gaussian process kernel is defined through a square matrix, \mathbf{K} (also called the covariance matrix), where each entry describes the covariance between two measurements.⁵⁰ We

⁴⁹ Documentation: <https://pychell.readthedocs.io/en/latest/>.

⁵⁰ See Haywood (2015) for a thorough discussion of Gaussian processes.

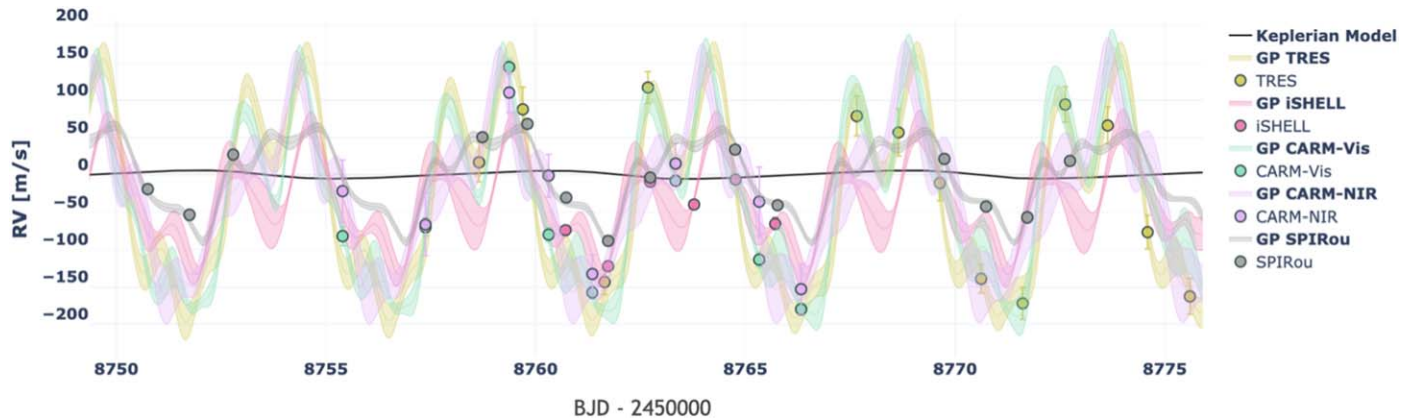


Figure 3. RVs of AU Mic zoomed in on a window with high-cadence, multiwavelength observations from 2019. Here, we use a disjoint QP GP kernel (Equation (1)) to model the stellar activity. Each plotted data set is only corrected according to the best-fit zero-points. Data errors are computed by adding the intrinsic errors in quadrature with any uncorrelated noise terms (i.e., 3 m s^{-1} for HIRES; see Table 2). Although each GP makes use of the same parameters, each still exhibits unique features. This indicates either an insufficient activity model with our cadence or yet-to-be characterized chromatic effects of activity from different wavelength regimes not consistent with a simple scaling relation.

introduce two GP kernels as extensions of the quasi-periodic (QP) kernel, which has been demonstrated in numerous cases to model rotationally modulated stellar activity in both photometric and RV observations (see Section 1).⁵¹

$$\mathbf{K}_{\text{QP}}(t_i, t_j) = \eta_{\sigma}^2 \exp \left[-\frac{\Delta t^2}{2\eta_{\tau}^2} - \frac{1}{2\eta_{\ell}^2} \sin^2 \left(\pi \frac{\Delta t}{\eta_p} \right) \right]$$

where $\Delta t = |t_i - t_j|$. (1)

Here, η_p typically represents the stellar-rotation period; η_{τ} the mean spot lifetime; η_{ℓ} is the relative contribution of the periodic term, which may be interpreted as a smoothing parameter (larger is smoother); and η_{σ} is the amplitude of the autocorrelation of the activity signal.

We seek to use a fully inclusive QP-like kernel that accounts for the wavelength-dependence of the stellar activity present in our multiwavelength data set. In this work, we only modify the amplitude parameter, η_{σ} ; we leave further chromatic modifications (namely, convective blueshift and limb-darkening; see Section 1) as subjects for future work. To first order, we expect the amplitude from activity to be linearly proportional to frequency (or inversely proportional to wavelength). This approximation is a direct result of the spot-contrast scaling with the photon frequency (or inversely with wavelength) from the ratio of two blackbody functions with different effective temperatures (Reiners et al. 2010).

We first reparameterize the amplitude through a linear kernel as follows:

$$\mathbf{K}_{\text{J1}}(t_i, t_j) = \eta_{\sigma, s(i)} \eta_{\sigma, s(j)} \times \exp[\dots]. (2)$$

Here, $\eta_{\sigma, s(i)} \eta_{\sigma, s(j)}$ are the effective amplitudes for the spectrographs at times t_i and t_j , respectively, where $s(i)$ represents an indexing set between the observations at time t_i and spectrograph s .⁵² Each amplitude is a free parameter.

We also consider a variation of this kernel that further enforces the expected inverse relationship between the

amplitude with wavelength. We rewrite the kernel to become:

$$\mathbf{K}_{\text{J2}}(t_i, t_j, \lambda_i, \lambda_j) = \eta_{\sigma, 0}^2 \left(\frac{\lambda_0}{\sqrt{\lambda_i \lambda_j}} \right)^{2\eta_{\lambda}} \times \exp[\dots]. (3)$$

Here, $\eta_{\sigma, 0}$ is the effective amplitude at $\lambda = \lambda_0$, and η_{λ} is an additional power-law scaling parameter with wavelength to allow for a more flexible nonlinear (with frequency) relation. λ_i and λ_j are the “effective” wavelengths for observations at times t_i and t_j , respectively. For both Equations (2) and (3), the expression within square brackets is identical to that in Equation (1).

To make predictions from \mathbf{K}_{J2} (Equation (3)), we follow Rasmussen & Williams (2006; their Equations (2.23) and (2.24)). We construct the matrix $\mathbf{K}_{\text{J2}}(t_{i,*}, t_j, \lambda_*, \lambda_j)$, which denotes the $n_* \times n$ matrix of the covariances evaluated at all pairs of test points and training points (the data). Wavelengths in the $*$ dimension are identical, and therefore each realization corresponds to a unique wavelength. This formulation allows us to realize the GP with high accuracy for all wavelengths so long as at least one wavelength is sampled near $t_{i,*}$. Predictions with kernel \mathbf{K}_{J1} (Equation (2)) are found in a similar fashion, where each realization corresponds to a particular spectrograph.

3.3. Primary RV Analyses

We first bin out-of-transit RV observations from each night (per spectrograph). While not negligible, we expect changes from rotationally modulated activity to be small within a night, so we choose to mitigate activity on shorter timescales our model is not intended to capture (e.g., p-mode oscillations, granulation). The median RV for each spectrograph is also subtracted. We choose to ignore poorly sampled regions with respect to our adopted mean spot lifetime η_{τ} (100 days; see Section 3.3.1). Each instance of a covariance matrix represents a family of functions, and therefore the GP regression may be too flexible (and thus poorly constrained) in regions of low-cadence observations. We also ignore regions with only low-precision measurements (median errors $\gtrsim 10 \text{ m s}^{-1}$). This limits our analyses to all observations between 2019 September and 2020 December, and the spectrographs HIRES, TRES, CARMENES-VIS and NIR, SPIRou, and iSHELL. We do

⁵¹ Other parameterizations are also common.

⁵² Truly simultaneous measurements (i.e., $t_i = t_j$) would necessitate a more sophisticated indexing set.

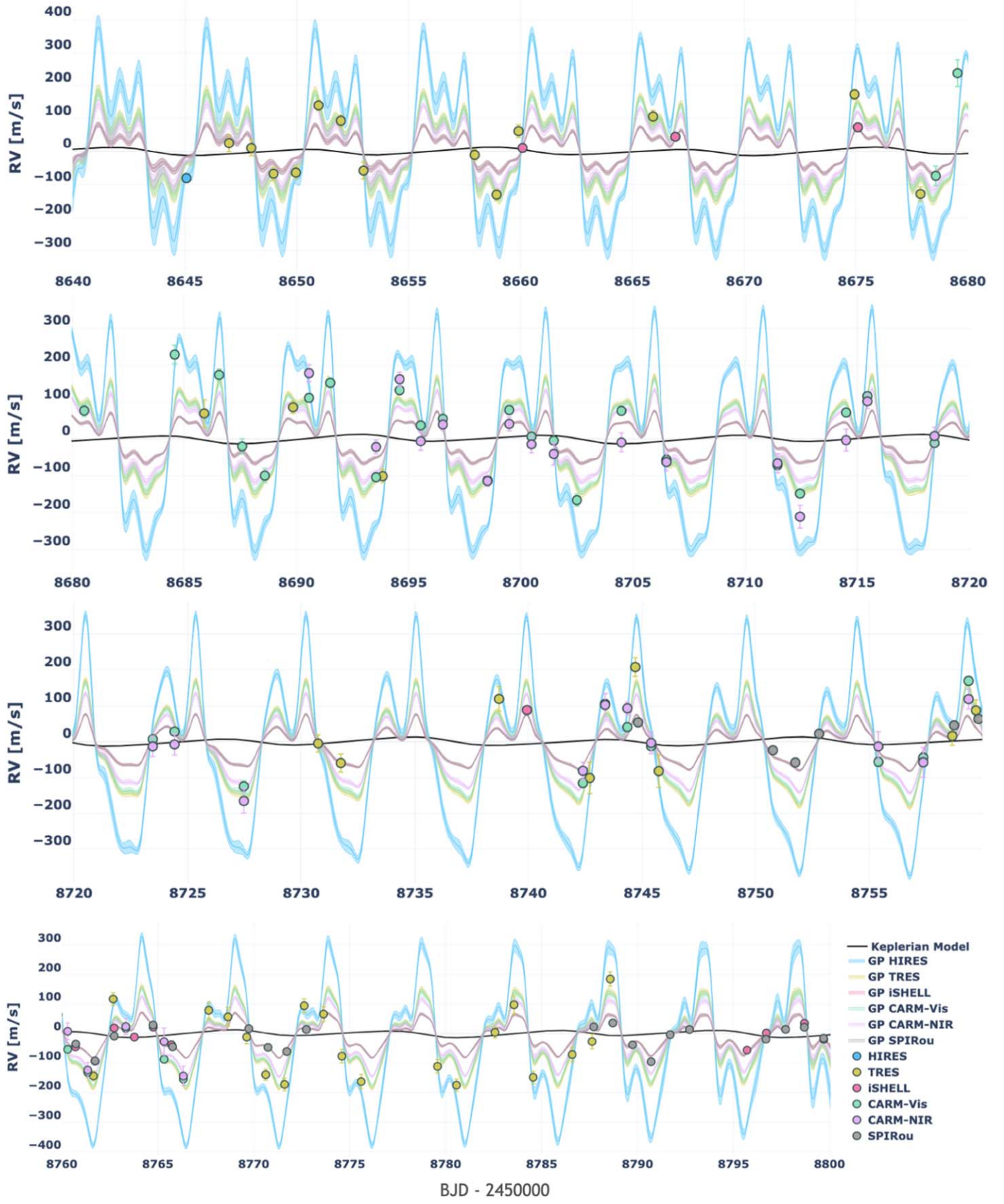


Figure 4. The 2019 RVs using kernel K_{J1} (Equation (2)) to model the stellar activity. Although there is only one HIRES observation in early 2019, we are still able to make predictions for the HIRES GP for the entire baseline by using joint kernels.

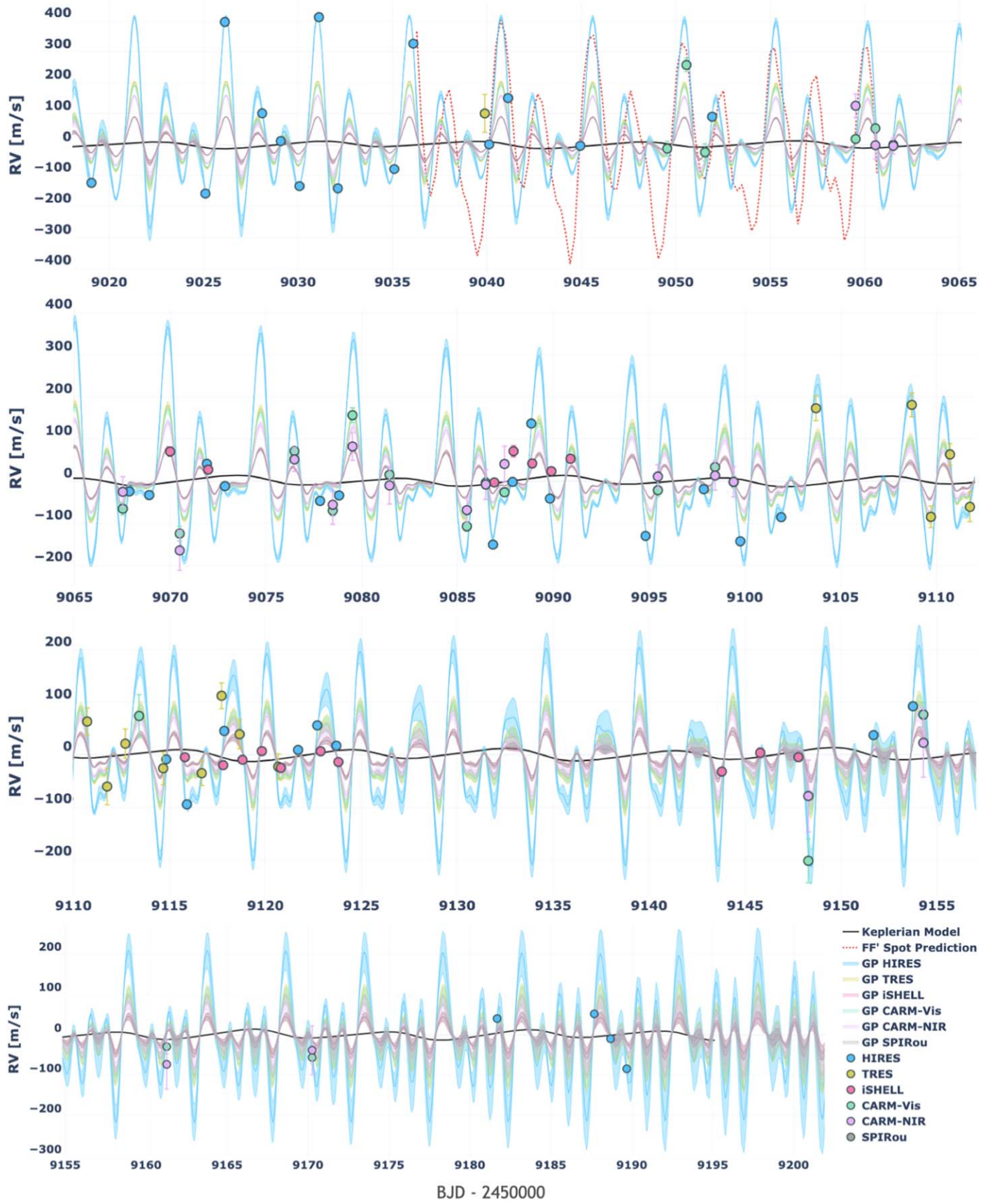


Figure 5. Same as Figure 4, but for our 2020 observations that overlap with the TESS Sector 27 photometry. In red, we show the generated FF' curve for spot-induced activity signals (Equation (5), arbitrarily scaled) generated from the TESS light curve (Section 3.3.1).

Table 2
The Model Parameters and Prior Distributions Used in Our Primary Fitting Routines

Parameter [units]	Initial Value (P_0)	Priors	Citation
P_b [days]	8.4629991	🔒	Primary transit; M21
TC_b [days]	2458330.39046	🔒	Primary transit; M21
e_b	0.189	$\mathcal{N}(P_0, 0.04)$	Secondary eclipse; K. L. Collins et al. (2021, in preparation)
ω_b [rad]	1.5449655	$\mathcal{N}(P_0, 0.004)$	Secondary eclipse; K. L. Collins et al. (2021, in preparation)
K_b [$m\ s^{-1}$]	8.5	Positive	K21
P_c [days]	18.858991	🔒	Primary transit; M21
TC_c [days]	2458342.2243	🔒	Primary transit; M21
e_c	0	🔒	...
ω_c [rad]	π	🔒	...
K_c [$m\ s^{-1}$]	5	Positive	M21
$\eta_{\sigma,0}$ [$m\ s^{-1}$]	216	$\mathcal{J}(1, 600), \mathcal{N}(P_0, 10)$	RVs; this work
η_{λ}	1.18	$\mathcal{U}(0.3, 2)$	RVs; this work
$\eta_{\sigma,\text{HIRES}}$ [$m\ s^{-1}$]	130	$\mathcal{J}(1, 600), \mathcal{N}(P_0, 30)$	RVs; this work
$\eta_{\sigma,\text{TRES}}$ [$m\ s^{-1}$]	103	$\mathcal{J}(1, 600), \mathcal{N}(P_0, 30)$	RVs; this work
$\eta_{\sigma,\text{CARM-VIS}}$ [$m\ s^{-1}$]	98	$\mathcal{J}(1, 600), \mathcal{N}(P_0, 30)$	RVs; this work
$\eta_{\sigma,\text{CARM-NIR}}$ [$m\ s^{-1}$]	80	$\mathcal{J}(1, 600), \mathcal{N}(P_0, 30)$	RVs; this work
$\eta_{\sigma,\text{SPIROu}}$ [$m\ s^{-1}$]	42	$\mathcal{J}(1, 600), \mathcal{N}(P_0, 30)$	RVs; this work
$\eta_{\sigma,\text{iSHELL}}$ [$m\ s^{-1}$]	40	$\mathcal{J}(1, 600), \mathcal{N}(P_0, 30)$	RVs; this work
η_{τ} [days]	100	🔒	TESS light curve and RVs; this work
η_{ℓ}	0.28	...	TESS light curve and RVs; this work
η_p [days]	4.836	$\mathcal{N}(P_0, 0.001)$	TESS light curve; this work
γ (per spectrograph) [$m\ s^{-1}$]	1	$\mathcal{U}(-300, 300), \mathcal{N}(0, 100)$	RVs; this work
σ_{HIRES} [$m\ s^{-1}$]	3	🔒	...
σ_{TRES} [$m\ s^{-1}$]	0	🔒	...
$\sigma_{\text{CARM-VIS}}$ [$m\ s^{-1}$]	0	🔒	...
$\sigma_{\text{CARM-NIR}}$ [$m\ s^{-1}$]	0	🔒	...
σ_{SPIROu} [$m\ s^{-1}$]	0	🔒	...
σ_{iSHELL} [$m\ s^{-1}$]	0	🔒	...
M_{\star} [M_{\odot}]	$0.5^{+0.03}_{-0.03}$...	P20
R_b [R_{\oplus}]	$4.38^{+0.18}_{-0.18}$...	P20
R_c [R_{\oplus}]	$3.51^{+0.16}_{-0.16}$...	M21

Note. Here, **🔒** indicates the parameter is fixed. We run models utilizing K_{J1} and K_{J2} . We list the radii of AU Mic b and c measured in M21 that we use to compute the corresponding densities of each planet.

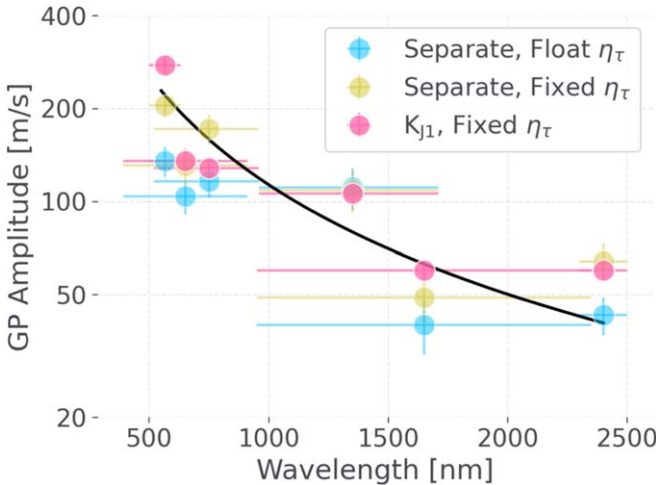


Figure 6. The best-fit GP amplitudes and uncertainties from kernels without enforcing any dependence with wavelength. We consider cases that let η_{τ} and η_{ℓ} float, as well as our fixed values (see Table 2). The solid line is a least-squares solution to the amplitudes for kernel K_{J2} (Equation (3)) for the joint-kernel fixed case (pink markers). Horizontal bars correspond to the adopted spectral range for each instrument.

not include six binned IRD or 13 binned MINERVA-Australis observations in our primary analyses, as we expect the offsets to be poorly constrained in the presence of stellar activity. Finally, we discard three CARMENES-VIS and 13 CARMENES-NIR measurements from our analyses, primarily near the beginning of each season, due to residuals $>100\ m\ s^{-1}$ that are inconsistent with our other data sets. We suspect that telluric contamination, which is further exacerbated by the high airmass of the observations, may have degraded the CARMENES observations. For completeness, we present fit results including all spectrographs in Appendix D. A summary of measurements is provided in Table 1.

Our RV model first consists of two Keplerian components for the known transiting planets, a GP model for stellar activity, and per-instrument zero points. The zero points are each assigned to $1\ m\ s^{-1}$ with a uniform prior of $\pm 300\ m\ s^{-1}$. We further adopt a normal prior of $\mathcal{N}(0, 100)$ to make each offset well-behaved. When using multiple priors, the composite prior probability for such a parameter will not integrate to unity. For the combination of a uniform + normal prior, this is not a concern; the normal prior is properly normalized and takes on a continuous range of values, whereas the uniform prior will either result in a constant term added

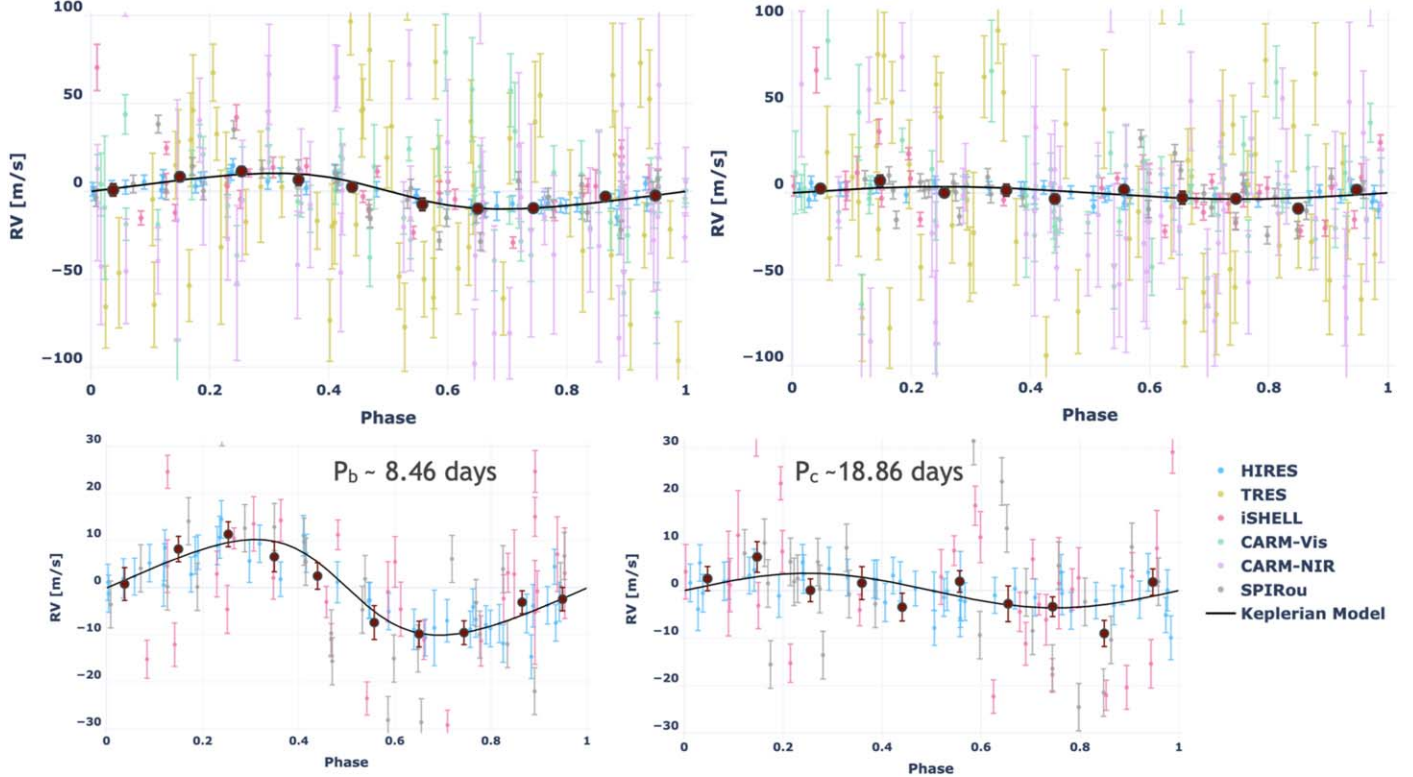


Figure 7. The phased RVs for AU Mic b (left column), and c (right column), and the corresponding best-fit Keplerian models, generated from our nominal two-planet model. For each spectrograph, we subtract the unique zero points, all other planet signals, and the appropriate GP. Corresponding data errors are computed by adding the intrinsic error in quadrature with additional uncorrelated noise (i.e., 3 m s^{-1} for HIRES; see Table 2). The dark red points are generated by binning the phased RVs using a window size of 0.1, weighted by $1/\sigma_{\text{RV}}^2$, where σ_{RV} are the data errors. In the top row, we plot all data used in the fit. In the bottom row, we only show HIRES, iSHELL, and SPIRou. Although the HIRES cadence in 2020 was relatively dense with respect to the activity timescales η_τ and η_P , the data still appear to be overfit.

to the likelihood function if the parameter is in bounds, or $-\infty$ if out of bounds.

Analyses of the TESS transits in M21 found $P_b = 8.4629991 \pm 0.0000024$ days, $\text{TC}_b = 2458330.39046 \pm 0.00016$, $P_c = 18.858991 \pm 0.00001$ days, and $\text{TC}_c = 2458342.2243 \pm 0.0003$. For all of our analyses, we fix P and TC for planets b and c; the uncertainties in these measurements are insignificant even for our full baseline of ≈ 17 yr. The semi-amplitudes of each planet start at $K_b = 8.5 \text{ m s}^{-1}$ and $K_c = 5 \text{ m s}^{-1}$, and are only enforced to be positive. Preliminary analyses of a secondary eclipse observed in Spitzer observations support a moderately eccentric orbit for AU Mic b, with $e_b = 0.189 \pm 0.04$ (K. I. Collins et al. 2021, in preparation), which is somewhat larger than the eccentricity determined from the duration of the primary transits observed with TESS ($e_b = 0.12 \pm 0.04$; Gilbert et al. 2021). We assume a circular orbit for AU Mic c, and further examine eccentric cases in Section 5.1. The Keplerian component of our RV model in `pychell` is nearly identical to that used in `RadVel` (Fulton et al. 2018). Kepler's equation is written in `Python` and makes use of the `numba.@njit` decorator (Lam et al. 2015) for optimal performance. We exclusively use the orbit basis $\{P, \text{TC}, e, \omega, K\}$.

Our optimizer seeks to maximize the natural logarithm of the a posteriori probability (MAP) under the assumption of normally distributed errors:

$$\ln \mathcal{L} = -\frac{1}{2}[\mathbf{r}^\top \mathbf{K}_o^{-1} \mathbf{r} + \ln |\mathbf{K}_o| + N \ln(2\pi)] + \sum_i \ln \mathcal{P}_i. \quad (4)$$

Here, \mathbf{r} is the vector of residuals between the observations and model, \mathbf{K}_o is the covariance matrix sampled at the same observations, N is the number of data points, and $\{\mathcal{P}_i\}$ is the set of prior knowledge. We maximize Equation (4) using the iterative Nelder–Mead algorithm described in Cale et al. (2019), which is included as part of the `optimize` package. We also sample the posterior distributions using the `emcee` package (Foreman-Mackey et al. 2013) for a subset of models to determine parameter uncertainties, always starting from the MAP-derived parameters. In all cases, we use twice the number of chains as varied parameters. We perform a burn-in phase of 1000 steps followed by a full MCMC analysis for $\approx 50 \times$ the median autocorrelation time (steps) of all chains.

3.3.1. Estimation of Kernel Parameters

We briefly analyze both sectors of TESS photometry in order to estimate the GP kernel parameters η_τ , η_ℓ , and η_P . We note that the rotationally modulated structure in both sectors is consistent (Figure 1). If we assume spots are spatially static in the rest frame of the stellar surface (i.e., spots do not migrate), this suggests a similar spot configuration and contrast for each sector. We first determine η_P by qualitatively analyzing both TESS sectors phased up to periods close to that used in M21 (4.862 ± 0.032 days) with a step size of 0.001 day (see Figure 1). We find $\eta_P \approx 4.836$ or $\eta_P \approx 4.869$ days from our range of periods tested; no periods between these two values are consistent with our assumption of an identical spot configuration. The difference in these two periods further corresponds to

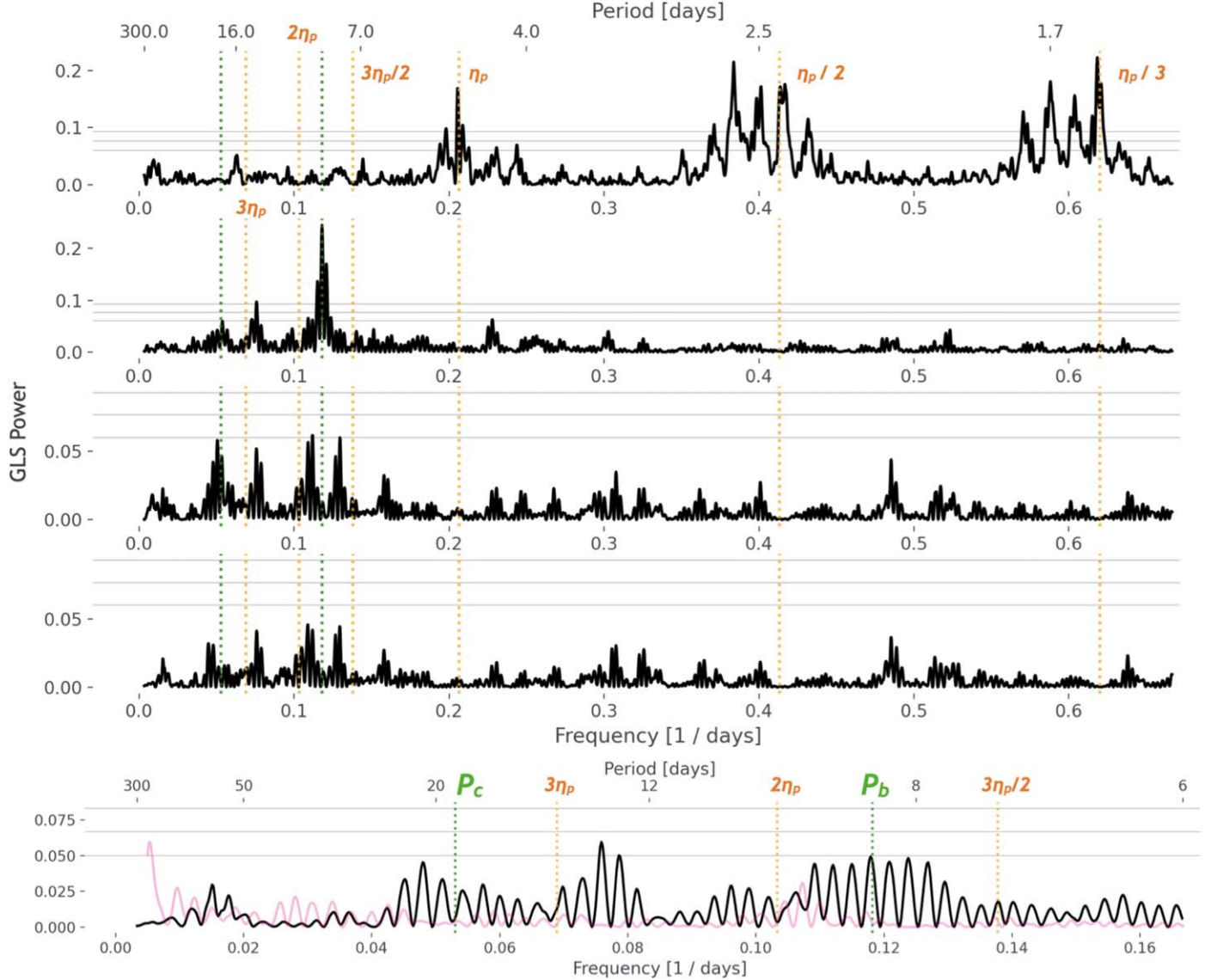


Figure 8. GLS periodograms for AU Mic. Rows 1–4 are generated from our nominal two-planet MAP fit result using K_{J_1} (Equation (2)) to model the stellar activity. From top to bottom, with each step applying an additional “correction,” we show: (1) zero-point corrected RVs, (2) activity-filtered RVs, (3) planet b–filtered RVs, and (4) planet c–filtered RVs. Annotated from left to right in green are the periods for AU Mic c and b. In the top row, we also annotate in orange (from left to right) potential aliases of the stellar rotation period $3\eta_p$, $2\eta_p$, and $3\eta_p/2$, followed by the first three harmonics. In the bottom row, we compute a periodogram from an activity-filtered and trend-corrected zero-planet model to indicate how power from planets is absorbed by the GP. In each periodogram, we also identify the FAP power levels corresponding to 0.1% (highest), 1%, and 10% (lowest). The clear alias present in all periodograms is caused from the large gap between the two seasons of observations. In the bottom panel, we also plot in pink a Lomb–Scargle periodogram (arbitrarily scaled) of our window function (i.e., identical yet arbitrary RVs at each observation).

one additional period between the two sectors (i.e., $|1/\eta_{p,1} - 1/\eta_{p,2}| \approx 1/700 \text{ day}^{-1}$). The smaller of these two values implies AU Mic b is in a 7:4 resonance with the stellar rotation period (Szabó et al. 2021), potentially indicating tidal interactions between the planet and star. We adopt $\eta_p \sim \mathcal{N}(4.836, 0.001)$ in all our analyses where the uncertainty is a conservative estimate determined by our step size.

Although the TESS light curve itself can provide insight into η_τ and η_ℓ , we instead try to estimate these values directly from the predicted spot-induced RV variability via the FF' technique (Aigrain et al. 2012):

$$\Delta RV_{\text{spots}}(t) = -F(t)F'(t)R_\star/f. \quad (5)$$

Here, F is the photometric flux and f represents the relative flux drop for a spot at the center of the stellar disk. To compute F and F' (the derivative of F with respect to time), we first fit the TESS

light curve via cubic spline regression (`scipy.interpolate.LSQUnivariateSpline`; Virtanen et al. 2020) for each sector individually, with knots sampled in units of 0.5 day ($\approx 10\%$ of one rotation period), to average over transits and the majority of flare events (Figure 1). The nominal cubic splines are then used to directly compute both F and F' on a downsampled grid of 100 evenly spaced points for each sector. We then divide the resulting joint-sector curve by its standard deviation for normalization; we do not care to directly fit for the chromatic parameter $f(\text{TESS}, \dots)$. We further assume f to be constant in time (i.e., spots are well-dispersed on the stellar surface). We then perform both MAP and MCMC analyses for this curve using a standard QP kernel (Equation (1)) with loose uniform priors of $\eta_\tau \sim \mathcal{U}(10, 2000)$ (days) and $\eta_\ell \sim \mathcal{U}(0.05, 0.6)$. We set the intrinsic error bars of the curve to zero but include an additional “jitter” (white noise)

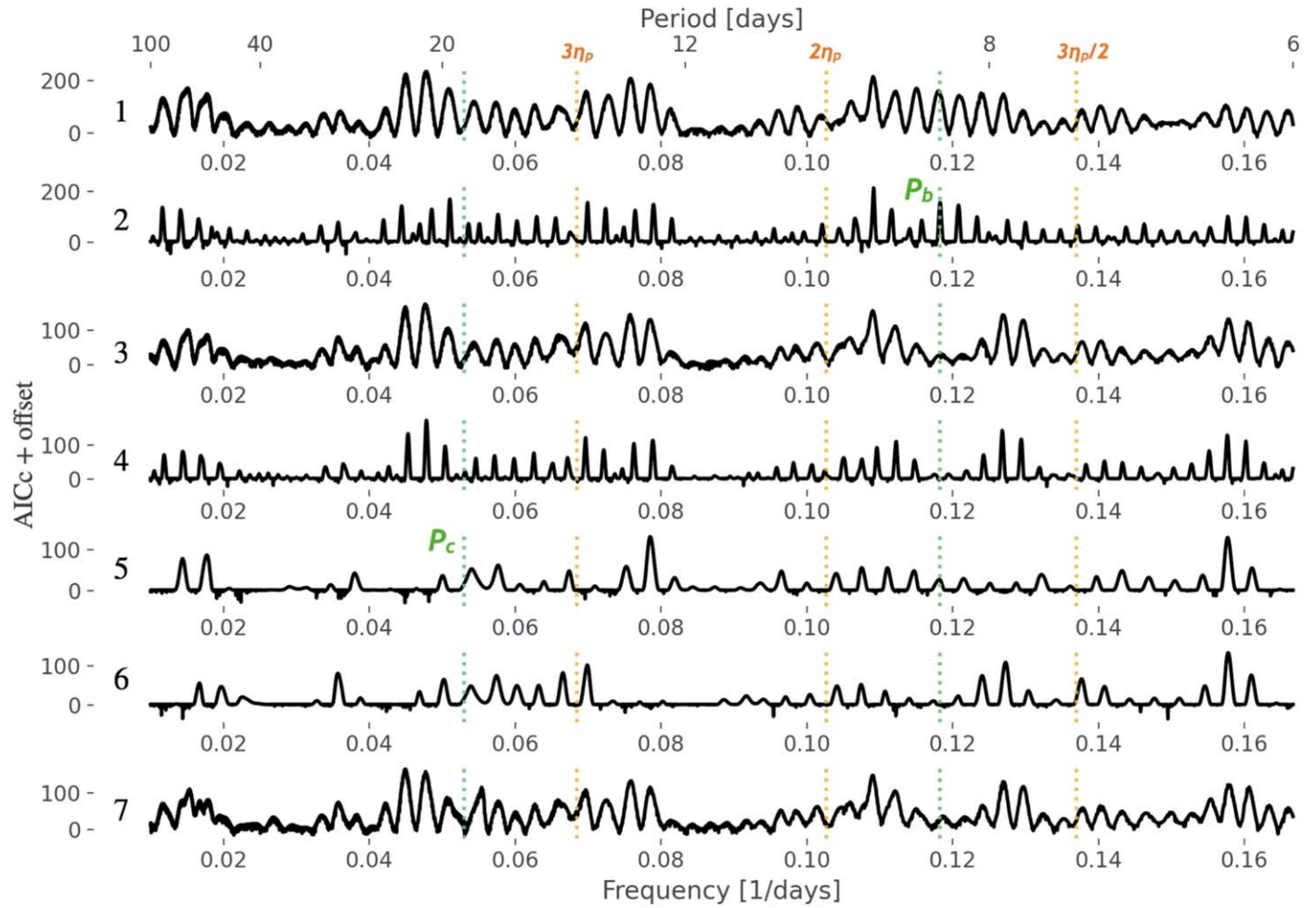


Figure 9. “Brute-force” periodograms for AU Mic with different assumptions for planetary models, but all making use of kernel K_{J1} (Equation (2)) to model the stellar activity. In each row, we perform a MAP fit for a wide range of fixed periods for a particular “test” planet. In row 1, we include no other planets in our model, and allow for the test planet’s TC to float. In row 2, we perform the same search but fixing TC to the nominal value for AU Mic b (Table 2). In row 3, we include a model for AU Mic b (with $K_b \sim \mathcal{N}(8.5, 2.5)$; see K21), and search for a second planet, again letting TC float. In rows 4–6, we perform the same search but fix the test planet’s TC to one of the three times of transit for AU Mic c from TESS (in chronological order). In the bottom row, we include nominal models for AU Mic b and c ($K_b \sim \mathcal{N}(8.5, 2.5)$, $K_c > 0$). We also annotate the same potential aliases with the stellar rotation period (orange) and planetary periods (green) as in Figure 8.

term in the model with a Jeffreys prior (Jeffreys 1946) distribution with the knee at zero to help keep the jitter well-behaved by discouraging larger values unless it significantly improves the fit quality through an inversely proportional penalty term. The amplitude of the model is drawn from a wide uniform distribution of $\mathcal{U}(0.3, 3.0)$. The posterior distributions are provided in Figure 2.

A fit to the FF' curve suggests a mean activity timescale $\eta_\tau \approx 92^{+29}_{-23}$ days. Although our interpretation implies η_τ should be comparable to the gap between the two sectors, (~ 700 days), we do not have photometric measurements between the two sectors, and therefore cannot speak to evolution that will be important for our 2019 observations. We further note that the TESS Sector 27 light curve exhibits moderate evolution whereas Sector 1 appears more stable (Figure 1). The posterior distributions are also consistent with a relatively smooth GP with the period length scale $\eta_\ell \approx 0.45 \pm 0.06$.

Before making use of our joint kernels, we first assess the performance of the standard QP kernel (Equation (1)) for each instrument individually. Here, each spectrograph makes use of a unique QP kernel and amplitude term, but the remaining three GP parameters are shared across all kernels. Each amplitude is

drawn from a normal prior with mean equal to the standard deviation of the data set, and a conservative width of 30 m s^{-1} . The expected semi-amplitudes for AU Mic b and c ($\lesssim 10 \text{ m s}^{-1}$) will negligibly affect this estimation. We also apply a Jeffreys prior with the knee at zero to help keep the amplitude well-behaved.⁵³ For η_τ and η_ℓ , we first make use of the same priors used to model the FF' curve. We further include a fixed jitter term at 3 m s^{-1} added in quadrature along the diagonal of the covariance matrix K_o for the HIRES observations only; HIRES observations provide the smallest intrinsic uncertainties, but are most impacted by activity (largest in amplitude), so we choose to moderately downweight the HIRES observations. Given the flexibility of GP regression with a nightly cadence, we choose not to fit for (nor include) jitter terms for other spectrographs, and further discuss this decision in Section 5.5. This is the most flexible model we employ to the RVs, and we therefore use these results to flag the aforementioned CARMENES-VIS and CARMENES-NIR measurements.

⁵³ Although the composite prior for the GP amplitudes is not proper (i.e., does not integrate to unity; see Section 3.3), we find nearly identical results with only the normal prior.

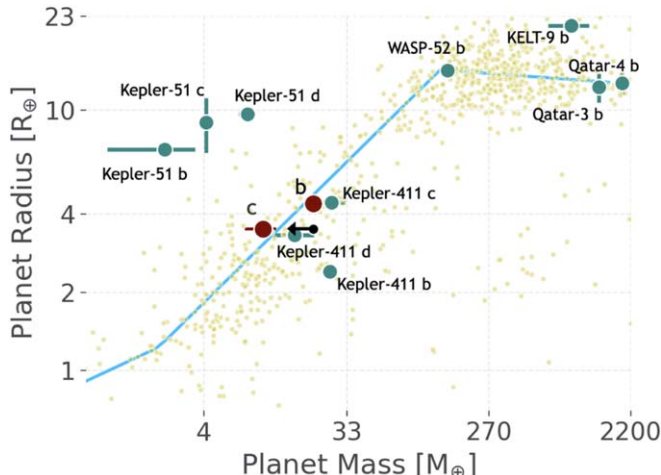


Figure 10. The mass vs. radius for all exoplanets with provided radii and masses from the NASA Exoplanet Archive (2019). For AU Mic b and c, we plot (maroon markers) the masses determined from our two-planet model with kernel \mathbf{K}_{J1} . We also indicate with an arrow the 5σ upper limit to the mass of AU Mic c determined from the posterior of K_c . The radii for b and c are those reported in M21. In blue, we plot a piecewise Chen-Kipping mass-radius relation (Chen & Kipping 2017). We also annotate (cyan markers) the masses and radii for a sample of young planets (estimated stellar age $\lesssim 400$ Myr).

We find normally distributed posteriors for η_τ and η_e (Figure 14), but the reduced χ^2 statistic of 0.32 indicates the model over fits the data. The per-spectrograph amplitudes are reasonably consistent with their respective priors, so we assert this is a result of η_τ (≈ 43 days) and/or η_e (≈ 0.23) taking on too small of values, indicating our RV model is insufficient to constrain these values from the RV observations, due to insufficient cadence and/or an inadequate model. We therefore again fix $\eta_\tau = 100$ days to let each season have mostly distinct activity models, while minimizing the flexibility within each season, which is consistent with what the FF' curve suggests. As a compromise between the FF' and RV analyses, we also fix $\eta_e = 0.28$. Our adopted value of η_τ is larger than that used in K21 (≈ 70 days⁵⁴), while η_e is nearly identical. We further explore these decisions and their impact on our derived semi-amplitudes in Section 5.2. With fixed value for η_τ , we rerun MAP and MCMC fits with disjoint kernels, yielding a reduced χ^2 of 0.86, indicating the model is now only slightly overfit.

3.3.2. Joint-kernel RV Fitting

We use results from the disjoint case to inform our primary joint-kernel models. Although the different GPs appear similar (Figure 3), each still exhibits unique features, suggesting a simple scaling is not valid and/or insufficient sampling for each kernel individually. Regardless, our two joint kernels will enforce a perfect scaling between any two spectrographs. The RVs are shown in Figures 4 and 5.

We run MAP and MCMC fits using the joint kernel \mathbf{K}_{J1} (Equation (2)) again making use of the same normal and Jeffreys priors for each amplitude. We then fit the resulting set of best-fit amplitudes using our proposed power-law relation (see Equation (3)): $\eta_o(\lambda) = \eta_{o,0}(\lambda_0/\lambda)^{\eta_\lambda}$ with `scipy.optimize.curve_fit` (Jones et al. 2001; Figure 6). We arbitrarily anchor λ_0 at $\lambda = 565$ nm. The effective mean wavelength of each spectrograph should consider the RV information content (stellar

and calibration), and ignore regions with dense telluric features. For gas-cell-calibrated spectrographs (HIRES, CHIRON, and iSHELL), we do limit the range to regions with gas-cell features. For all other spectrographs, we take the effective RV information content to be uniform over the full spectral range as a “zeroth-order” approximation (Reiners & Zechmeister 2020). We further do not consider regions of tellurics that may have been masked (e.g., CARMENES RVs generated with `serval`). Although these estimations are imperfect, they are only relevant to kernel \mathbf{K}_{J2} (Equation (3)). The adopted wavelengths for each spectrograph are listed in Table 1.

We find $\eta_{o,0} \approx 221$ m s⁻¹, and $\eta_\lambda \approx 1.17$. This amplitude is significantly larger than the intrinsic scatter of our observations (namely HIRES) suggests, so we adopt a tight normal prior of $\mathcal{N}(221, 10)$ to restrict it from getting any larger. We only apply a loose uniform prior for $\eta_\lambda \sim \mathcal{U}(0.2, 2)$. We then run corresponding MAP and MCMC fits with kernel \mathbf{K}_{J2} (Equation (3)). A summary of all parameters is provided in Table 2. We present and discuss fit results from both joint kernels in Section 4.

4. Results

The best-fit parameters and corresponding uncertainties from the MAP and MCMC analyses with a two-planet model using joint kernels \mathbf{K}_{J1} (Equation (2)) and \mathbf{K}_{J2} (Equation (3)) are provided in Table 3. We compute planet masses, densities, and orbital semimajor axes by propagating the appropriate MCMC chains. The uncertainties in M_* and the planetary radii from Table 2 are added in quadrature where appropriate. Corner plots presenting the posterior distributions of each varied parameter are provided in Figures 16 and 17 for kernels \mathbf{K}_{J1} and \mathbf{K}_{J2} , respectively. All chains are well-converged, with posteriors resembling Gaussian distributions. We find the offsets for each spectrograph are highly correlated with one another; we note this is unique to the cases leveraging a joint kernel, and strongest when data sets overlap, but we do not further explore this result.

Unlike kernel \mathbf{K}_{J2} , \mathbf{K}_{J1} only enforces a scaling relation between the different spectrographs, but no correlation with wavelength, so we adopt results from \mathbf{K}_{J1} for our primary results, although the results for K_b and K_c are moderately consistent between kernels. With kernel \mathbf{K}_{J1} (Equation (2)), we report the median semi-amplitudes of AU Mic b and c to be $10.23^{+0.88}_{-0.91}$ m s⁻¹ and $3.68^{+0.87}_{-0.86}$ m s⁻¹, corresponding to masses of $20.12^{+1.57}_{-1.72}$ M_\oplus and $9.60^{+2.07}_{-2.31}$ M_\oplus , respectively. The phased-up RVs for AU Mic b and c are shown in Figure 7. With kernel \mathbf{K}_{J2} (Equation (3)), we find $K_b = 8.92^{+0.85}_{-0.85}$ m s⁻¹ and $K_c = 5.21^{+0.90}_{-0.87}$ m s⁻¹. Both our findings for K_b are larger but within 1σ of the semi-amplitude reported in K21 ($8.5^{+2.3}_{-2.2}$ m s⁻¹). The mass of AU Mic c is also consistent with a Chen-Kipping mass-radius relation ($\approx 12.1 M_\oplus$; Chen & Kipping 2017). The posterior distributions for e_b and ω_b are also consistent with their respective priors. Our finding for K_b is nearly twice as large as that obtained when using disjoint QP kernels (5.58 m s⁻¹; Figure 15), although the uncertainties are similar. With disjoint kernels, we find no evidence in the RVs for AU Mic c.

We further validate our results by computing the Bayesian information criterion (BIC) and the small-sample Akaike information criterion (Akaike 1974; Burnham & Anderson 2002). We compute the relevant quantities for a power set of planet models. We are not trying to independently detect the eccentricity of AU Mic b, and therefore we do not include cases with $e_b = 0$. Prior probabilities are not included in the calculation of the

⁵⁴ In K21, the hyperparameters η_τ and η_e absorb the factors of two present in the formulation used in this work (Equation (1)).

Table 3
Best-fit Parameters and Corresponding Keplerian Variables for Our Primary Two-planet Fits Using Joint Kernels K_{J1} (Equation (2)) and K_{J2} (Equation (3))

Name [units]	MAP (J1)	MCMC (J1)	MAP (J2)	MCMC (J2)
P_b [days]	8.4629991
TC _b [days; BJD]	2458330.39046
e_b	0.187	$0.186^{+0.036}_{-0.035}$	0.182	$0.181^{+0.035}_{-0.035}$
ω_b [radians]	1.5452	$1.5451^{+0.0038}_{-0.0038}$	1.5453	$1.5454^{+0.0041}_{-0.0041}$
K_b [m s ⁻¹]	10.21	$10.23^{+0.88}_{-0.91}$	8.94	$8.92^{+0.85}_{-0.85}$
M_b [M_\oplus]	20.14	$20.12^{+1.57}_{-1.72}$	17.66	$17.73^{+1.68}_{-1.62}$
a_b [au]	0.0645	$0.0645^{+0.0013}_{-0.0013}$
ρ_b [g cm ⁻³]	1.32	$1.32^{+0.19}_{-0.20}$	1.16	$1.16^{+0.18}_{-0.18}$
P_c [days]	18.858991
TC _c [days; BJD]	2458342.2243
e_c	0
ω_c [radians]	π
K_c [m s ⁻¹]	3.62	$3.68^{+0.87}_{-0.86}$	5.23	$5.21^{+0.90}_{-0.87}$
M_c [M_\oplus]	9.50	$9.60^{+2.07}_{-2.31}$	13.71	$14.12^{+2.48}_{-2.71}$
a_c [au]	0.1101	$0.1101^{+0.002}_{-0.002}$
ρ_c [g cm ⁻³]	1.21	$1.22^{+0.26}_{-0.29}$	1.75	$1.80^{+0.31}_{-0.34}$
γ_{HIRES} [m s ⁻¹]	2.9	$4.1^{+55.6}_{-57.0}$	-19.4	$-8.7^{+43.3}_{-42.9}$
γ_{TRES} [m s ⁻¹]	11.4	$12.1^{+27.4}_{-27.8}$	-0.2	$9.3^{+38.4}_{-38.0}$
$\gamma_{\text{CARM-VIS}}$ [m s ⁻¹]	3.7	$4.3^{+26.0}_{-26.6}$	-12.1	$-3.4^{+34.5}_{-33.9}$
$\gamma_{\text{CARM-NIR}}$ [m s ⁻¹]	2.6	$2.9^{+21.7}_{-21.8}$	-6.8	$-1.5^{+21.2}_{-21.2}$
γ_{SPIRou} [m s ⁻¹]	5.5	$5.6^{+12.3}_{-12.4}$	0.72	$5.1^{+17.8}_{-17.3}$
γ_{iSHELL} [m s ⁻¹]	-2.8	$-2.4^{+12.1}_{-12.4}$	-7.5	$-4.3^{+13.0}_{-12.9}$
$\eta_{\sigma,0}$ [m s ⁻¹]	242.4	$243.1^{+8.8}_{-9.1}$
η_λ	0.843	$0.845^{+0.024}_{-0.024}$
$\eta_{\sigma,\text{HIRES}}$ [m s ⁻¹]	269.4	$275.7^{+17.4}_{-16.4}$
$\eta_{\sigma,\text{TRES}}$ [m s ⁻¹]	132.3	$135.4^{+10.6}_{-9.5}$
$\eta_{\sigma,\text{CARM-VIS}}$ [m s ⁻¹]	125.1	$128.2^{+8.8}_{-8.2}$
$\eta_{\sigma,\text{CARM-NIR}}$ [m s ⁻¹]	103.0	$105.5^{+9.1}_{-8.7}$
$\eta_{\sigma,\text{SPIRou}}$ [m s ⁻¹]	58.5	$60.1^{+4.3}_{-4.0}$
$\eta_{\sigma,\text{iSHELL}}$ [m s ⁻¹]	58.5	$60.0^{+4.2}_{-3.9}$
η_P [days]	4.8384	$4.8384^{+0.0008}_{-0.0009}$	4.8376	$4.8376^{+0.0009}_{-0.0009}$

Note. The MCMC values correspond to the 15.9th, 50th, and 84.1th percentiles. Planet masses, densities, and semimajor axes are computed by propagating the appropriate MCMC chains. We also add in quadrature the uncertainties in M_* and planetary radii from Table 2 where relevant.

corresponding $\ln \mathcal{L}$ (Equation (4)), to maintain normalization between different models. The results are summarized in Table 4 and are consistent with the relative precisions for each derived semi-amplitude.

Finally, we compute and present the reduced chi-squared statistic (χ^2_{red}) for each spectrograph individually to assess their respective goodness of fit (Table 5). We add in quadrature the intrinsic error bars with any additional uncorrelated noise (i.e., 3 m s⁻¹ for HIRES; see Table 2). We find the HIRES observations are moderately overfit ($\chi^2_{\text{red}} = 0.64$), whereas the other spectrographs are underfit. We suspect this is due to the activity amplitude for HIRES being significantly larger than the other spectrographs despite exhibiting a similar overall dispersion. Although we include an additional 3 m s⁻¹ white noise term for the HIRES observations, they still yield the smallest overall error bars and therefore are given the most weight in the GP regression. Although a more flexible uncorrelated noise model may yield a more accurate weighting scheme for the different spectrographs (i.e., a varied “jitter” parameter for each spectrograph), we favor the model without them for the variety of reasons discussed in Section 5.5. Finally, we note that we find moderately similar results when

not using the HIRES RVs altogether ($K_b = 12.95 \pm 1.1$ m s⁻¹, $K_c = 3.5 \pm 1.0$ m s⁻¹).

4.1. Evidence For Additional Candidates?

We compute periodograms to further assess the relative statistical confidence of the two transiting planets and to search for other planets in the system. We first compute a series of generalized Lomb–Scargle (GLS; Zechmeister & Kürster 2018; Czesla et al. 2019) periodograms out to 500 days after removing the nominal zero points, appropriate GPs, and the two planets, all generated using parameters from our nominal two-planet model (Table 3) with kernel K_{J1} (Equation (2)) to model the stellar activity. We also compute an activity-filtered periodogram from a planet-free model to assess how much the GP model will absorb planetary signals, and inform our interpretation of other peaks present in the periodogram. We further plot the normalized power levels for false-alarm probabilities (FAPs) of 10%, 1%, and 0.1%.

We also compute “brute-force” periodograms by performing MAP fits for a wide range of fixed orbital periods for a user-defined “test planet” with various assumptions for other model

Table 4

Model Information Criterion for AU Mic b and c Using Kernel \mathbf{K}_{J1} (Equation (2)) to Model the Stellar Activity

Planets	$\ln \mathcal{L}$	χ^2_{red}	N Free	ΔAICc	ΔBIC
b, c	-1753.1	4.73	17	0	0
b	-1762.0	4.77	16	15.5	12.2
c	-1816.4	5.14	14	119.8	109.8
None	-1828.8	5.23	13	142.4	129.13

Table 5

Reduced χ^2 for Each Spectrograph from Our Nominal Two-planet Model Using Kernel \mathbf{K}_{J1}

Spectrograph	χ^2_{red}
HIRES	1.09
TRES	6.86
CARMENES-VIS	5.89
CARMENES-NIR	4.39
SPIRou	16.70
iSHELL	22.43

Note. Unlike when using quasi-disjoint kernels (Section 3.3.1), we find the model is overall underfit with the joint kernel. We suspect this is primarily due to an inadequate stellar-activity (i.e., a scaling relation is insufficient between spectrographs) and/or the exclusion of per-spectrograph jitter terms, and discuss these details further in Section 5.5.

parameters (see Addison et al. 2021). Given the time complexity of GP regression, we only consider periods out to 100 days. We first run two searches with no other planets in the model, first allowing for the test planet’s TC to float, and second fixing TC to the nominal value for AU Mic b (Table 3). We then run searches for a second planet, this time including a planetary model to account for the orbit of AU Mic b, with $K_b \sim \mathcal{N}(8.5, 2.5)$, consistent with the semi-amplitude found in K21. We again consider the case of letting the test planet’s TC float, then run three cases with fixing the test planet’s TC to each time of transit for AU Mic c from the TESS Sector 1 and 27 light curves (M21). Last, we perform a search for a third planet, letting its TC float, and including models for AU Mic b and c ($K_b \sim \mathcal{N}(8.5, 2.5)$, $K_c > 0$).

Both the GLS (Figure 8) and brute-force (Figure 9) periodograms exhibit clear aliasing with a frequency of ≈ 0.00281 days⁻¹ (or 356 days), which we attribute to having two seasons of observations separated by ≈ 200 days. Given the respective power of AU Mic b in both the GLS and brute-force planet-free periodograms, we briefly explore other peaks with similar power, even though all other peaks are below all three FAPs after removing the nominal two-planet model (Figure 8, row 3; Figure 9, row 7). Both two- and zero-planet periodograms (as well as GLS and brute-force) show power between the orbits of AU Mic b and c near 12.72 and 13.19 days, as well as power near 66.7 days for the residual RVs. Although these peaks are comparable in power to AU Mic b in both planet-free periodograms, they may be spurious. We further discuss the confirmation of AU Mic b and c as well as the validation of such additional potential candidates in Section 5.3. A mass-radius diagram is shown in Figure 10 to place the mass and radius of all AU Mic b and c in context with other known exoplanets, including a subset of young sample of exoplanets shown in P20. The plotted masses for AU Mic b and c are from our nominal two-planet model using kernel \mathbf{K}_{J1} (Equation (2)).

Table 6

MCMC Results with Different Assumptions for the Mean Spot Lifetime η_τ and η_ℓ Using Kernel \mathbf{K}_{J1} (Equation (2))

η_τ (days)	η_ℓ	K_b (m s ⁻¹)	K_c (m s ⁻¹)	χ^2_{red}
40	0.15	8.79 ± 1.47	7.38 ± 1.65	1.58
40	0.2	8.84 ± 1.30	8.51 ± 1.33	2.10
40	0.25	8.23 ± 1.17	9.05 ± 1.17	2.45
40	0.3	7.41 ± 1.08	9.13 ± 1.13	2.68
40	0.35	6.95 ± 0.98	9.23 ± 1.05	2.85
70	0.15	8.74 ± 1.24	6.88 ± 1.30	1.99
70	0.2	10.32 ± 1.13	5.90 ± 1.07	2.69
70	0.25	10.45 ± 1.04	4.76 ± 0.95	3.25
70	0.3	9.61 ± 0.91	4.16 ± 0.89	3.65
70	0.35	9.18 ± 0.82	3.94 ± 0.83	3.90
100	0.15	9.28 ± 1.17	5.88 ± 1.08	2.46
100	0.2	10.85 ± 1.00	4.73 ± 0.98	3.20
100	0.25	10.78 ± 0.95	3.78 ± 0.87	3.76
100	0.3	9.81 ± 0.85	3.63 ± 0.80	4.12
100	0.35	9.22 ± 0.80	3.60 ± 0.77	4.39
200	0.15	9.38 ± 0.98	4.01 ± 0.96	3.44
200	0.2	11.04 ± 0.89	3.35 ± 0.84	4.16
200	0.25	11.09 ± 0.87	3.38 ± 0.77	4.73
200	0.3	10.14 ± 0.84	4.51 ± 0.76	5.28
200	0.35	9.06 ± 0.73	4.77 ± 0.66	5.59
300	0.15	9.32 ± 0.92	3.84 ± 0.87	3.82
300	0.2	10.60 ± 0.88	3.78 ± 0.81	4.68
300	0.25	10.42 ± 0.80	4.99 ± 0.74	5.59
300	0.3	10.51 ± 0.76	4.52 ± 0.68	5.96
300	0.35	9.89 ± 0.75	4.41 ± 0.68	6.27

Note. For each row, we fix the values of η_τ and η_ℓ . All other model parameters take on the initial values and priors from Table 2 for a two-planet model. We perform a MAP fit followed by MCMC sampling for each case. We report the nominal values and uncertainties for the semi-amplitudes of AU Mic b and c from the MCMC fitting, as well as the reduced chi-squared statistic, χ^2_{red} , using the MAP-derived parameters. Uncertainties reported here for K_b and K_c are the average of the upper and lower uncertainties.

5. Discussion

5.1. Constraints on Eccentricity

Here, we briefly explore eccentric orbits for the two-transiting planets b and c. For each planet, we take $e \sim \mathcal{U}(0, 0.7)$ and $\omega \sim \mathcal{U}(0, 2\pi)$. We only use kernel \mathbf{K}_{J1} (Equation (2)) to model the stellar activity. Posterior distributions are presented in Figure 18. We find $e_b = 0.30 \pm 0.04$, which is $\approx 50\%$ larger than our prior informed by a secondary eclipse event indicates. The corresponding finding of $\omega_b = 3.01 \pm 0.27$ is also inconsistent with our adopted prior for ω_b . The posterior distribution for e_c is concentrated at the upper bound (0.7), implying an overlapping orbit with AU Mic b. Orbital stability calculations presented in M21 indicate $e_c < 0.2$, so we assert our model is unable to accurately constrain its eccentricity. The behavior of e_c further indicates our detection of K_c may not be significant.

5.2. Sensitivity to Kernel Hyperparameters

Our analyses in Section 3.3.1 make use of a fixed mean spot lifetime $\eta_\tau = 100$ days and smoothing parameter $\eta_\ell = 0.28$. Here, we determine how sensitive the recovered semi-amplitudes of AU Mic b and c are to these two parameters. We consider $\eta_\tau \in \{40, 70, 100, 200, 300\}$ (days), and $\eta_\ell \in \{0.15, 0.2, 0.25, 0.3, 0.35\}$.

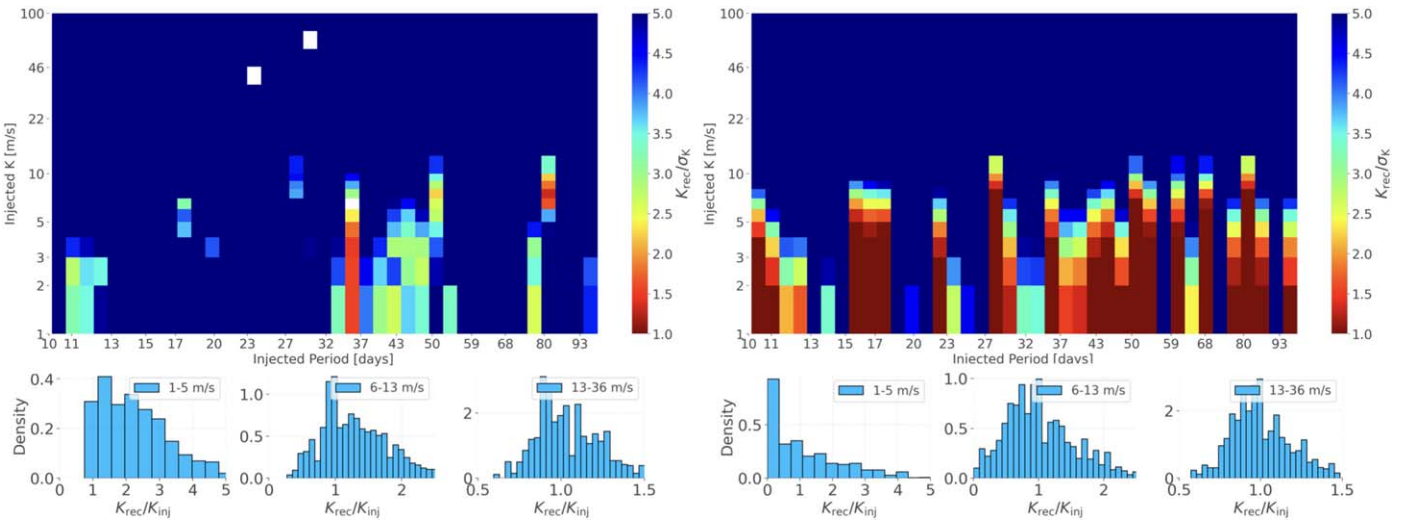


Figure 11. Histograms depicting our injection and recovery test results. In the top row, we show the relative confidence interval of the recovered semi-amplitudes (K_{rec}) derived from the MCMC analysis in the case of letting the ephemeris (P , TC) float (left) and fixing the ephemeris to the injected values (right). In the bottom row, we compare the recovered semi-amplitude to the injected value (K_{inj}).

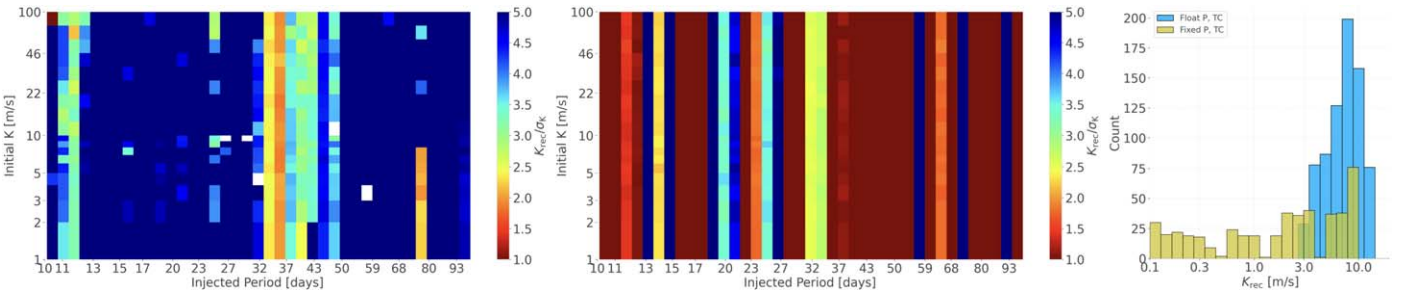


Figure 12. Histograms depicting the recovery of planetary signals without having injected any into the data. In panels 1 and 2, we show the relative confidence interval of the recovered semi-amplitudes (K_{rec}) derived from the MCMC analysis in the case of letting the ephemeris (P , TC) float (left) and fixing the ephemeris to the arbitrary $\text{TC} = 2457147.36589$ (middle). On the right, we show the recovered semi-amplitudes for each case.

We perform MAP and MCMC fits for all pairs of these two fixed parameters using $\mathbf{K}_{\mathbf{J}1}$ (Equation (2)) for a two-planet model. All other parameters adopt initial values and priors from Table 2. Results are summarized in Table 6.

We find K_b is only moderately sensitive to the values of each hyperparameter, ranging from ~ 7 to 11 m s^{-1} . With a larger spot lifetime, K_b tends toward larger values, indicating the GP is likely absorbing power from planet b with a more flexible model (smaller η_τ). However, K_b is relatively insensitive to the value of η_ℓ . The range of values for K_c is larger, changing by nearly a factor of three. Unlike K_b , K_c is more unstable and tends toward larger values when using a more flexible (smaller) spot lifetime. The reduced chi-squared statistic indicates the model is not overfit in any of the cases performed, but is also larger than unity by a several factors in most cases, indicating our modeling is inadequate.

5.3. Planet Injection and Recovery

Here, we assess the fidelity of our RV model applied to the AU Mic system through planetary injection and recovery tests. We first inject planetary signals into the RV data with well-defined semi-amplitudes, periods, and ephemerides (TC). We arbitrarily choose $\text{TC} = 2457147.36589$ for all injected cases. We consider 40 unique periods between 5.12345 and 100.12345 days, uniformly distributed in log space. For the

semi-amplitude K , we consider values from 1 to 10 m s^{-1} with a step size of 1 m s^{-1} , as well as values between 10 and 100 m s^{-1} that are uniformly distributed in log space (20 total values). In all cases, we include a model for AU Mic b with fixed P and TC such that $K_b \sim \mathcal{N}(8.5, 2.5)$. We first assess our recovery capabilities using a Gaussian prior for P such that $P \sim \mathcal{N}(P_{\text{inj}}, P_{\text{inj}}/50)$ and a uniform prior for TC such that $\text{TC} \sim \mathcal{U}(\text{TC}_{\text{inj}} \pm P_{\text{inj}}/2)$. For each injected planet (one at a time), we run our MAP and MCMC analyses to determine the recovered K and corresponding uncertainty. The starting values for K and TC are always the injected values. We also consider the same injection and recovery test but with P and TC fixed to the injected value. We finally determine how susceptible our RV model is to pick out “fake” planets by running these same two trials with no injected planets. Although there are no injected planets, we still run the same trials as for the injected case with different initial values for K . A two-dimensional histogram of the recovered K as a fraction of the injected K , as well as the associated uncertainty (also as a fraction of the injected K) for each case are shown in Figures 11 and 12 for the injected and non-injected cases, respectively.

In the case of injected planets, we find our RV model is able to confidently recover semi-amplitudes down to a few m s^{-1} in this data set with a relative precision of $\gtrsim 4\sigma$. However, a closer inspection reveals the recovered semi-amplitudes are typically

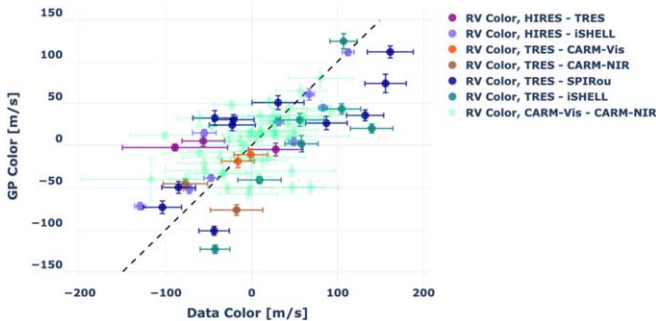


Figure 13. The observed “RV color” = $\text{RV}(t, \lambda) - \text{RV}(t, \lambda')$ ($\lambda' > \lambda$) from our 2019 and 2020 nights with nearly simultaneous measurements at unique wavelengths. These are plotted against the same RV-color difference predicted by our chromatic GP model using kernel K_{J2} . Pairs consisting of CARMENES-VIS and CARMENES-NIR measurements are nearly transparent, to make other pairs more visible. We do not plot pairs of SPIRou and iSHELL, because they are tightly centered near zero. A dashed one-to-one line is also shown. The weighted coefficient of determination (R^2) is ≈ 0.68 .

larger than the injected K , in particular for smaller injected values ($1\text{--}5 \text{ m s}^{-1}$) that include our measured semi-amplitude AU Mic c. When the ephemeris is known, we tend to poorly measure the smallest values of K , indicating the recovered TC in the non-fixed case is unlikely what we have injected. In the $6\text{--}13 \text{ m s}^{-1}$ range, which covers the recovered semi-amplitude of AU Mic b, we find that the accuracy of the recovered semi-amplitudes are $\sim 50\%$. So, while we quote a formal precision on the mass of AU Mic b to be $M_b = 20.12^{+1.72}_{-1.57} M_\oplus$ ($\sim 9\%$ precision), our injection and recovery tests indicate that the accuracy on the mass of AU Mic b is only known to a factor of two.

Unfortunately, attempts to recover non-injected planets are “unsuccessful,” in that our modeling finds strong evidence for planets we did not inject (Figure 12) in the case of allowing P and TC to float. A deeper investigation into the posteriors of such fits indicates certain parameters (primarily P and TC) are typically not well-behaved and yield non-Gaussian distributions. When fixing P and TC to “nominal” values, our modeling does not tend to find such nonexistent planets (Figure 12).

The confident recoveries of “fake” planets in our tests indicate our GP model is flexible enough to find relatively (quasi)-stable islands in probability space with high confidence for K specifically. Although several peaks stand out in our periodogram analyses (Figures 8 and 9), more observations and/or more sophisticated modeling are needed to robustly claim these periods as statistically validated planets. We further note that the recovered values of K for the smallest injected values are inaccurate, indicating our measurement of $K_c = 3.68 \text{ m s}^{-1}$ is also moderately unconvincing, and is likely an overestimate given the behavior of all recoveries at this level of K . We finally note this analysis is limited by planets we do not account for in the model, which may impact our ability to recover certain combinations of P and TC. Further tests using several values for the injected TC may also yield different results. With these limitations in mind, we also provide an estimation of the upper limit to the mass of AU Mic c. We find a 5σ upper limit to the semi-amplitude of AU Mic c of $\leq 7.68 \text{ m s}^{-1}$, corresponding to a mass of $\leq 20.13 M_\oplus$.

5.4. Utility of RV Color

Our chromatic kernel used in this work is an initial step to exploit the expected correlation of stellar activity versus wavelength by introducing a scaling relation between

wavelengths (Equations (2) and (3)). Here, we examine the “RV color” for our multiwavelength data set in order to further assess the correlation between our RVs with expected activity:

$$\text{RV}_{\text{color}}(t, \lambda, \lambda') = \text{RV}(t, \lambda) - \text{RV}(t, \lambda'). \quad (6)$$

We first determine which nights contain nearly simultaneous measurements at unique wavelengths. We require observations to be within 0.3 day ($\approx 6\%$ of one rotation period) of each other, in order to minimize differences from rotationally modulated activity but increase the number of pairs for our brief use. For each nearly simultaneous chromatic pair, we compute the “data color” directly from the measured RVs as well as the “GP color” by computing the differences between the two measurements and two GPs sampled at the identical times, respectively (such that $\lambda' > \lambda$). This calculation requires knowledge of the parameters in order to remove the per-instrument zero points and realize each appropriate GP, so we make use of the MAP-derived parameters in Table 3 with kernel K_{J2} (Equation (3)). The correlation between the data and GP color is shown in Figure 13. The agreement between the data and the model (weighted $R^2 \approx 0.71$) indicates that our chromatic GP technique is doing a good job of reproducing the RV-color phenomenon for multiple wavelength pairs.

With a sufficient model for stellar activity, we expect the data and GP RV color to match (up to white noise). Therefore, the “RV color” between the data and GP may be used to further constrain (in future analyses) the model (and therefore prevent overfitting) by including an effective L2 regularization penalty as follows:

$$\ln \mathcal{L} += -\Lambda \sum_t r_{\text{col}}(t)^2. \quad (7)$$

Here, r_{col} is the vector of residuals between the GP and data RV color, $\Lambda > 0$ is a tunable hyperparameter whose value is directly correlated with the relative importance and confidence of the stellar activity model, and $+$ = represents the standard “addition assignment” operator. The vector r_{col} may be computed for all pairs of wavelengths with (nearly) simultaneous measurements, and each pair can make use of identical or unique values of Λ . We finally note this regularization term is not limited to our assumption of a simple scaling relation, and could also be used in the case of disjoint kernels.

5.5. Additional Caveats and Future Work

Kernels K_{J1} (2) and K_{J2} (Equation (3)) make use of a scaling relation for stellar activity models at different wavelengths (spectrographs) where each activity model is drawn from a Gaussian process characterized by a covariance matrix utilizing all observations. Using such joint kernels yields fits with larger scatter than cases using disjoint QP kernels (one per spectrograph; Equation (1)). In the latter case, we find that although each of the activity models appear to be “in-phase” with one another, each GP exhibits unique features that are inconsistent with a simple scaling relation (Figure 3). With nightly sampling, it is difficult to determine whether the observed differences between disjoint GPs are indicative of inadequate sampling or an inadequate RV model (activity + planets). Further, all activity models used in this work make use of identical kernel hyperparameters (excluding the amplitude), which may further be an inadequate assumption. We expect the stellar rotation period (η_P) to be identical across wavelengths (or nearly so); however, it is not clear whether the mean

activity timescale (η_r) or period length scale (η_ℓ) in particular should be achromatic hyperparameters.

Our work further excluded per-spectrograph uncorrelated “jitter” terms. We suspect this may be the source of our model’s ability to find planets we did not inject into the model (Section 5.3), which we defer to future work. The reduced χ^2 values in Tables 4 and 6 quantify the degree to which our models do not capture signals from possible additional planets, incorrect values for eccentricity and/or ω , per-spectrograph systematics not included in the formal measurement uncertainties, stellar activity such as p-mode oscillations, convection noise, or longer timescale variations. Therefore, although our specific likelihood function (Equation (4)) assumes normally distributed errors, we choose not to combine any remaining (i.e., unaccounted for by the provided error bars) potentially correlated noise into an additional uncorrelated jitter term to keep our model simple.

More accurately characterizing the masses and orbits of AU Mic b and c may require a more sophisticated stellar activity model and more intensive multiwavelength cadence. Our work further does not make use of activity indicators (e.g., Ca II H and K, H α) or asymmetries in the cross-correlation function (e.g., the bisector inverse slope (BIS) or differential line width dLW; Zechmeister et al. 2018) to help constrain the activity model (see Rajpaul et al. 2015). The serval pipeline in particular provides a measure of the chromaticity (CRX) for both the CARMENES-VIS and NIR data sets, which we do not use in our modeling. For AU Mic, we expect that each spectrograph is precise enough to resolve first-order chromatic effects within their respective spectral grasp’s, which unfortunately will make the formal uncertainties of each spectrograph larger. Further, our QP-based kernels are primarily intended to capture rotationally modulated activity induced by temperature inhomogeneities on the stellar surface. Although the flexibility of disjoint GPs likely captures other rotationally modulated effects such as convective blueshift and limb-darkening, it will not capture short-term activity such as flares. We finally note that more seasons with high-cadence RVs will help mitigate the strong 1 yr alias present in our data set, and will help determine the correct periods for potential non-transiting planets.

6. Conclusion

In this work, we have developed two joint Gaussian process kernels that begin to take into account the expected wavelength dependence of stellar activity through a simple scaling relation. We apply our kernels to a data set of AU Mic, which is composed of RVs from multiple facilities, and wavelengths ranging from visible to K -band. With our analyses, we report a refined mass of AU Mic b of $M_b = 20.12^{+1.57}_{-1.72} M_\oplus$, and provide a 4.2σ mass estimate of the recently validated transiting planet AU Mic c to be $M_c = 9.60^{+2.07}_{-2.31} M_\oplus$, corresponding to a 5σ upper limit of $M_c \leq 20.13 M_\oplus$. We also identify additional peaks present in the activity-filtered RVs, but such periods require more evidence for a robust validation, given the overall flexibility of our RV model with an unknown ephemeris.

In Section 5.1, we find our model is unable to robustly constrain the eccentricity for AU Mic b or c. In Section 5.2, we find the derived planetary semi-amplitudes for AU Mic b and c are moderately sensitive to the choice of kernel parameters, indicating careful attention must be made when interpreting planetary masses with such a flexible model. Through injection

and recovery tests in Section 5.3, we further validate our RV model by demonstrating our ability to recover planets down to $\approx 10 \text{ m s}^{-1}$ when the orbit’s ephemeris is known. However, we find that the accuracy in the recovered semi-amplitudes is $\sim 50\%$ at 10 m s^{-1} . In Section 5.4, we introduce a method to further leverage the “RV color” correlation between the observations and activity model through penalizing the objective function by including an effective L2 regularization term.

All data processed with `pychell` (iSHELL and CHIRON) were run on ARGO, a research computing cluster provided by the Office of Research Computing, and the exo computer cluster, both at George Mason University, VA.

We thank all support astronomers, observers, and engineers from all facilities in helping enable the collection of the data presented in this paper.

The authors wish to recognize and acknowledge the very significant cultural role and reverence that the summit of Maunakea has always had within the indigenous Hawaiian community, where the iSHELL, HIRES, IRD, and SPIRou observations were recorded. We are most fortunate to have the opportunity to conduct observations from this mountain.

This work is supported by grants to Peter Plavchan from NASA (awards 80NSSC20K0251 and 80NSSC21K0349), the National Science Foundation (Astronomy and Astrophysics grants 1716202 and 2006517), and the Mount Cuba Astronomical Foundation.

Emily A. Gilbert also wishes to thank the LSSTC Data Science Fellowship Program, which is funded by LSSTC, NSF Cybertraining Grant #1829740, the Brinson Foundation, and the Moore Foundation; her participation in the program has benefited this work. Emily is thankful for support from GSFC Sellers Exoplanet Environments Collaboration (SEEC), which is funded by the NASA Planetary Science Division’s Internal Scientist Funding Model. The material is based upon work supported by NASA under award number 80GSFC21M0002.

This work is partly supported by JSPS KAKENHI grant No. JP18H05439, JST PRESTO grant No. JPMJPR1775, the Astrobiology Center of National Institutes of Natural Sciences (NINS) (grant No. AB031010).

M.T. is supported by JSPS KAKENHI grant Nos. 18H05442, 15H02063, and 22000005.

The authors also with to acknowledge funding from the Agencia Estatal de Investigación del Ministerio de Ciencia e Innovación (AEI-MCINN) under grant PID2019-109522GB-C53.

The authors also wish to thank the California Planet Search (CPS) collaboration for carrying out the HIRES observations recorded in 2020 presented in this work.

MINERVA-Australis is supported by Australian Research Council LIEF Grant LE160100001, Discovery Grant DP180100972, Mount Cuba Astronomical Foundation, and institutional partners University of Southern Queensland, UNSW Australia, MIT, Nanjing University, George Mason University, University of Louisville, University of California Riverside, University of Florida, and The University of Texas at Austin.

CARMENES is an instrument at the Centro Astronómico Hispano-Alemán de Calar Alto (CAHA, Almería, Spain). CARMENES is funded by the German Max-Planck-Gesellschaft (MPG), the Spanish Consejo Superior de Investigaciones Científicas (CSIC), the European Union

through FEDER/ERF FICTS-2011-02 funds, and the members of the CARMENES Consortium (Max-Planck-Institut für Astronomie, Instituto de Astrofísica de Andalucía, Landessternwarte Koenigstuhl, Institut de Ciències de l’Espai, Institut für Astrophysik Göttingen, Universidad Complutense de Madrid, Thüringer Landessternwarte Tautenburg, Instituto de Astrofísica de Canarias, Hamburger Sternwarte, Centro de Astrobiología and Centro Astronómico Hispano-Alemán), with additional contributions by the Spanish Ministry of Economy, the German Science Foundation through the Major Research Instrumentation Programme and DFG Research Unit FOR2544 “Blue Planets around Red Stars,” the Klaus Tschira Stiftung, the states of Baden-Württemberg and Niedersachsen, and by the Junta de Andalucía.

We acknowledge financial support from the Agencia Estatal de Investigación of the Ministerio de Ciencia, Innovación y Universidades and the ERDF through projects PID2019-109522GB-C5[1:4]/AEI/10.13039/501100011033, PGC2018-098153-B-C33, and the Centre of Excellence “Severo Ochoa” and “María de Maeztu” awards to the Instituto de Astrofísica de Canarias (CEX2019-000920-S), Instituto de Astrofísica de Andalucía (SEV-2017-0709), and Centro de Astrobiología (MDM-2017-0737), and the Generalitat de Catalunya/CERCA program.

This paper includes data collected by the NASA TESS mission that are publicly available from the Mikulski Archive for Space Telescopes (MAST). Funding for the TESS mission

is provided by NASA’s Science Mission Directorate. We acknowledge the use of public TESS data from pipelines at the TESS Science Office and at the TESS Science Processing Operations Center (Jenkins et al. 2016).

Baptiste Klein acknowledges funding from the European Research Council under the European Union’s Horizon 2020 research and innovation program (grant agreement No. 865624, GPRV).

Eder Martioli acknowledges funding from the French National Research Agency (ANR) under contract number ANR-18-CE31-0019 (SPaSH).

Software: pycell (Cale et al. 2019), optimize,⁵⁵ Matplotlib (Hunter 2007), SciPy (Virtanen et al. 2020), NumPy (Harris et al. 2020), Numba (Lam et al. 2015), corner (Foreman-Mackey et al. 2020), plotly (Inc., 2015), Gadfly Matplotlib theme <https://gist.github.com/JonnyCBB/c464d302fefce4722fe6cf5f46114ea>, emcee, (Foreman-Mackey et al. 2013).

Appendix A Posterior Distributions

Here, we show the posterior distributions for the relevant RV models employed in this work. In each corner plot, blue lines correspond to the 50th percentile of the distribution. Upper and lower uncertainties correspond to the 84.1st and 15.9th percentiles, respectively.

⁵⁵ <https://optimize.readthedocs.io/en/latest/>

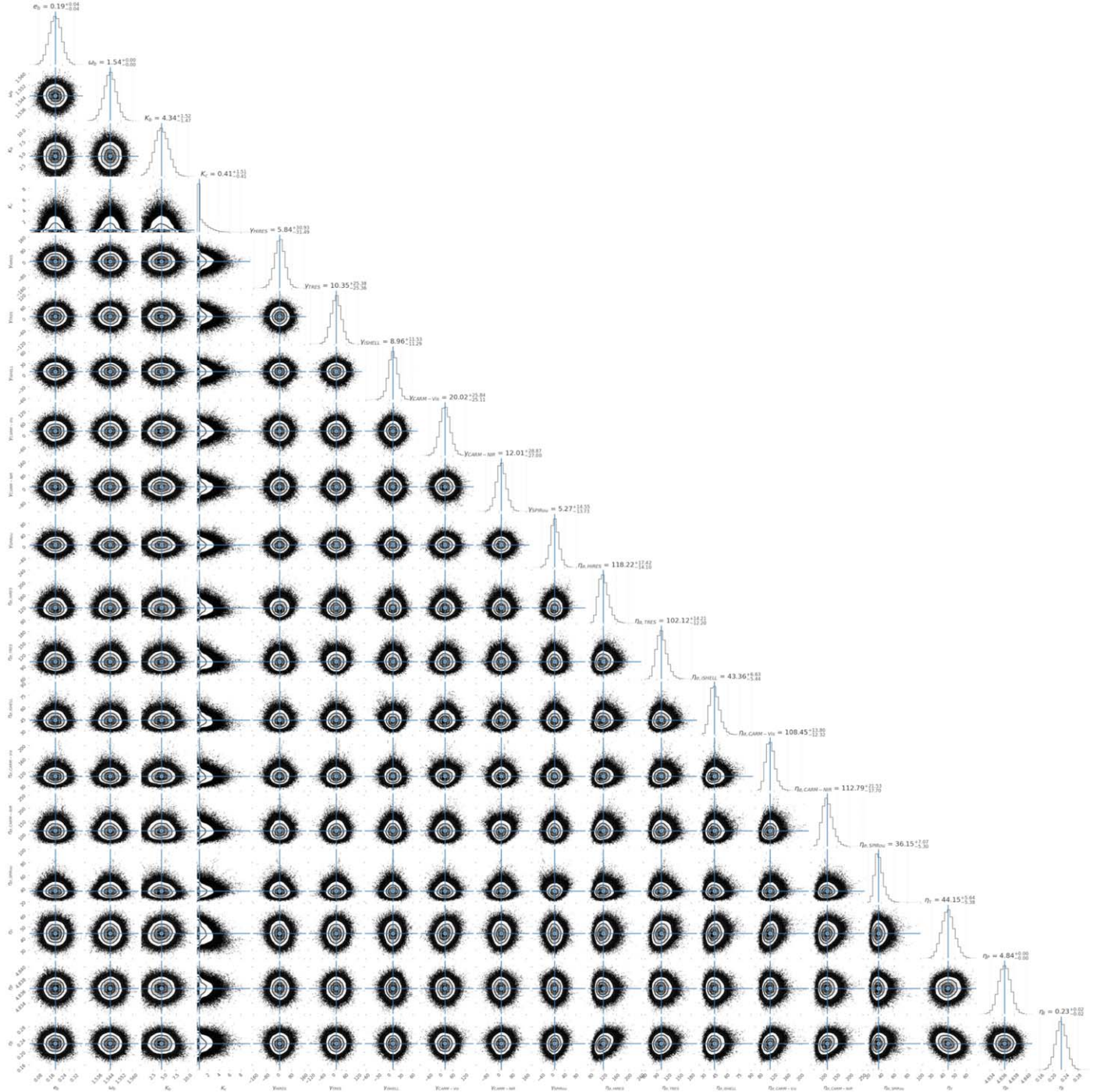


Figure 14. Posterior distributions using disjoint QP kernels (Equation (1)) for each spectrograph to model the stellar activity, including a two-planet model for the transiting planets b and c. The derived values for η_t and η_ℓ suggest a more dynamic activity model than the FF' curve prediction suggests.

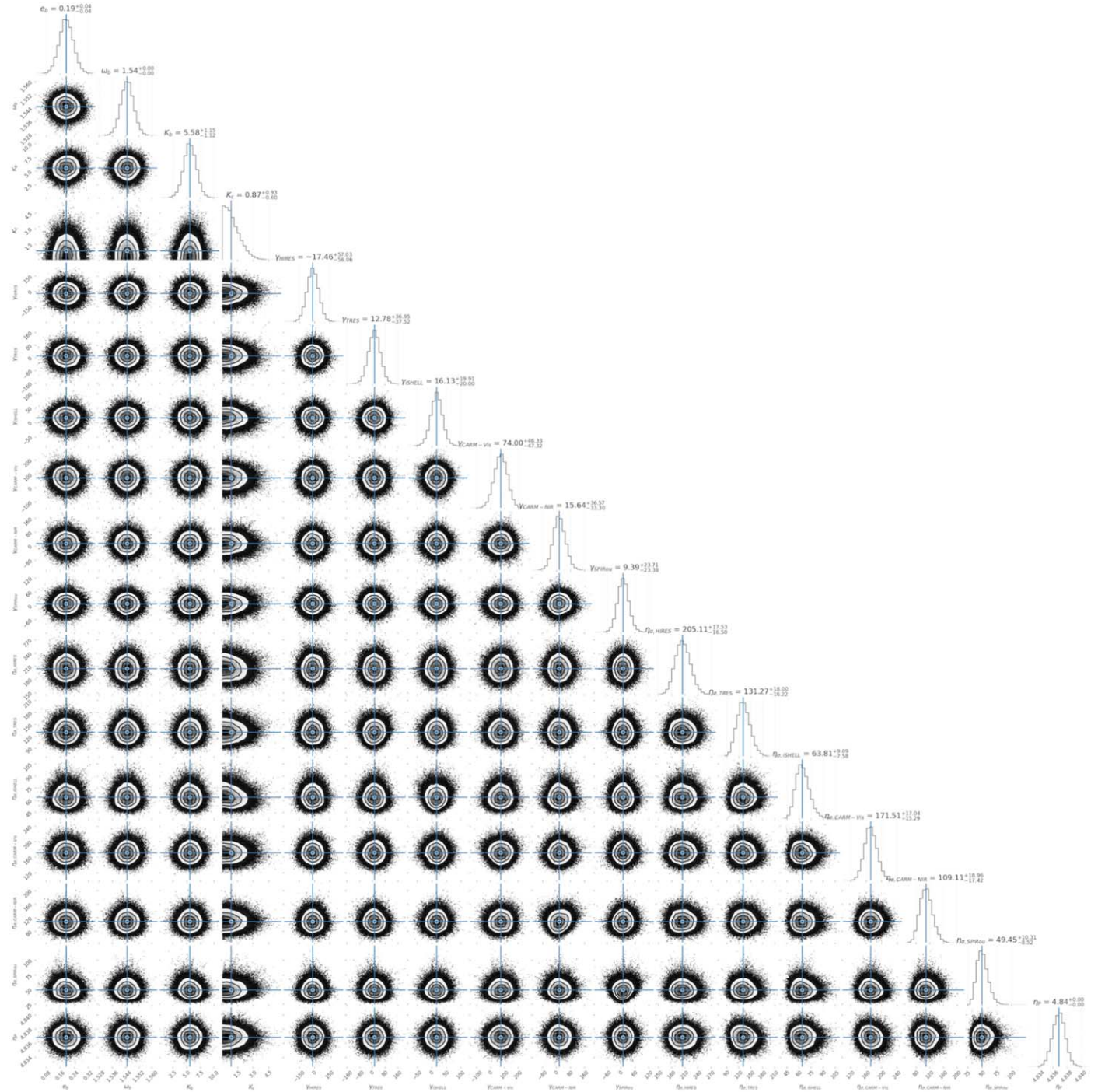


Figure 15. Same as Figure 14, but fixing $\eta_r = 100$ days and $\eta_e = 0.28$.

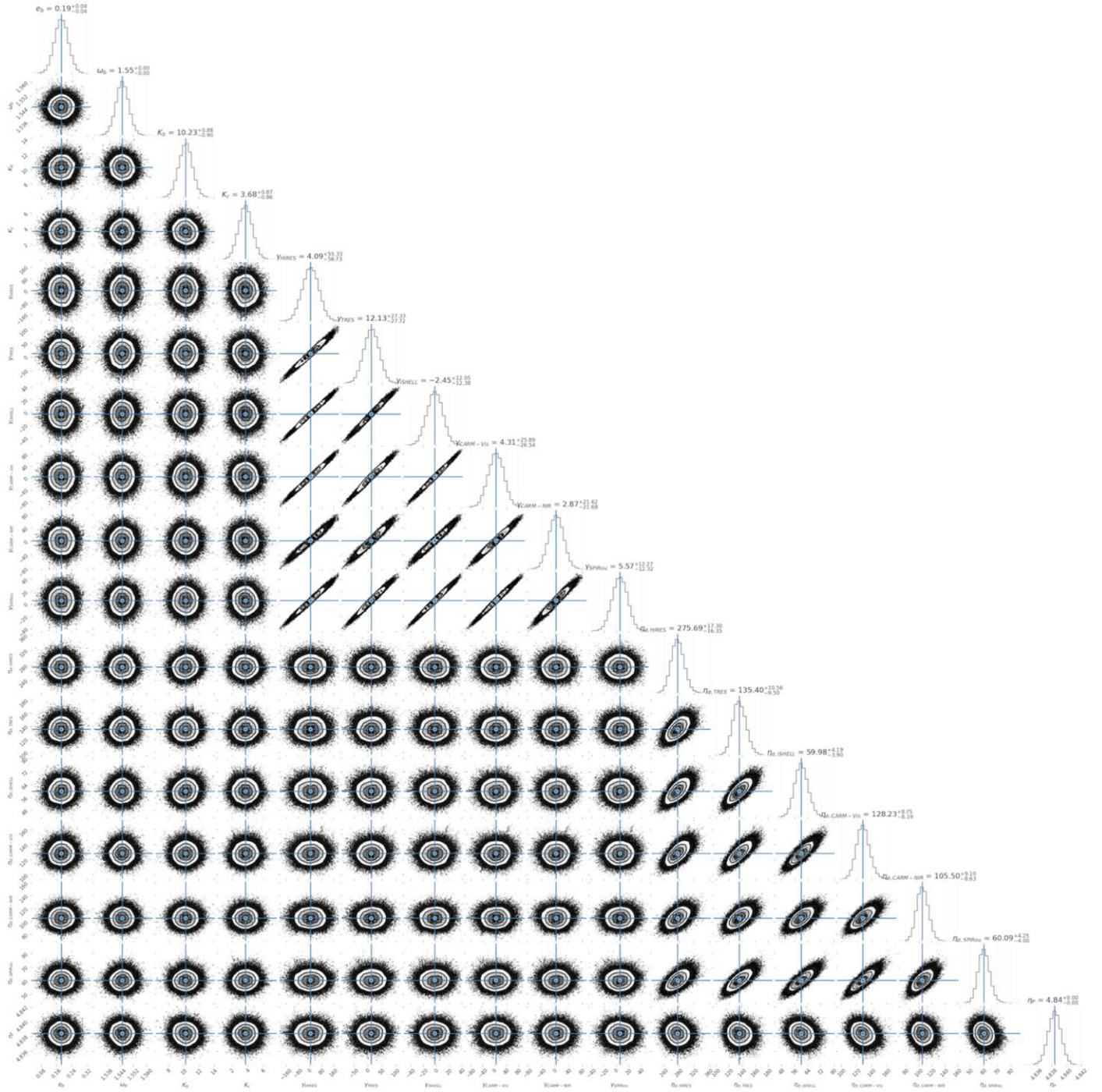


Figure 16. Posterior distributions for a two-planet fit to the RVs using K_{J1} (Equation (2)) to model the stellar activity.

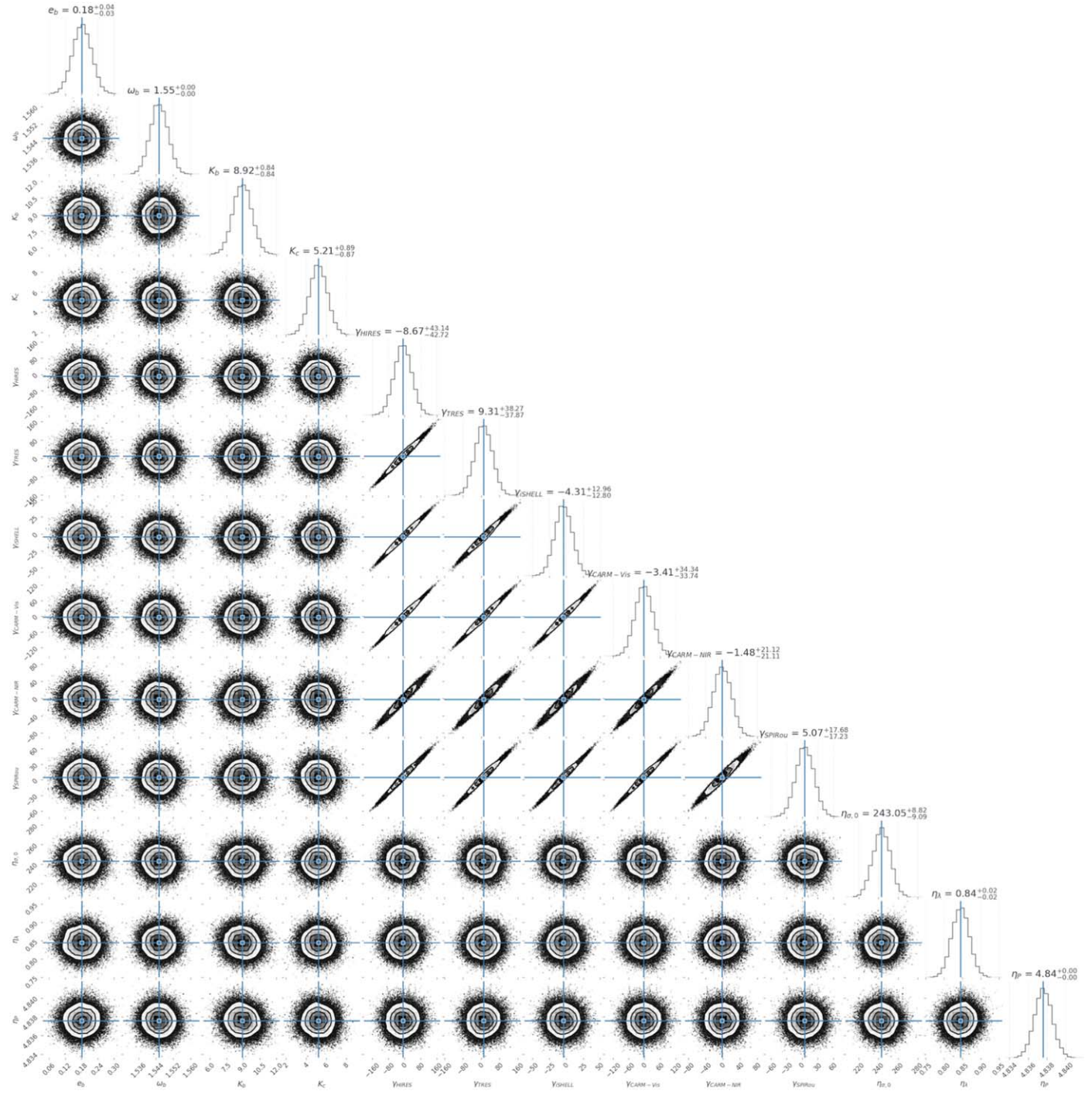


Figure 17. Same as Figure 16, but using K_{J2} to model the stellar activity.

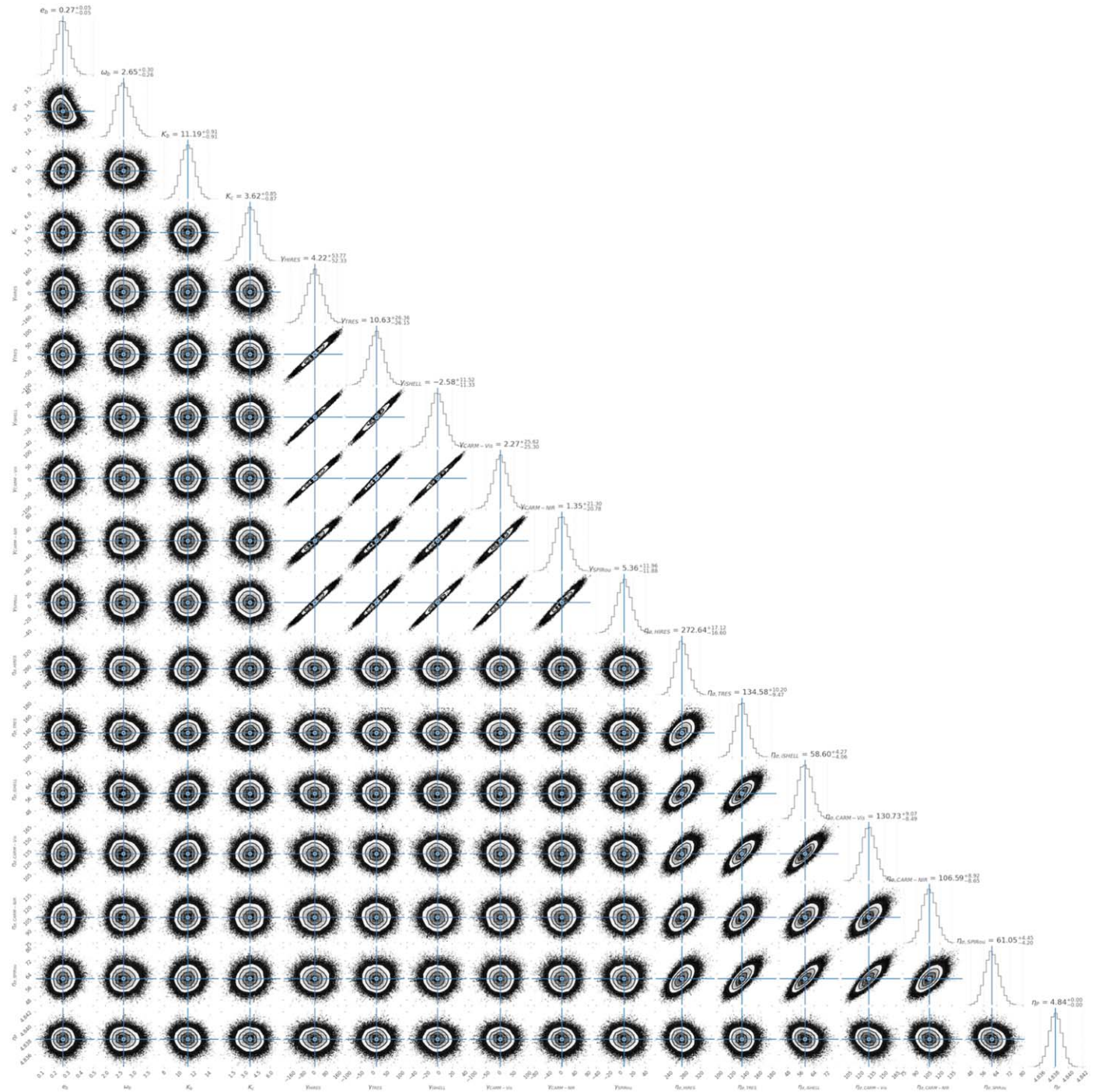


Figure 18. Same as Figure 16, but using less restrictive priors for e_b and ω_b as well as e_c and ω_c .

Appendix B

Optimize

`Optimize`⁵⁶ is a generic, high-level optimization package in *Python*, which generalizes the Bayesian-inspired classes used in `RadVel`. The primary container (*Python* class) in `optimize` is referred to as an “`OptProblem`;” primary attributes for this object are then helper types to (1) construct the model, (2) compare the data and model with an objective function, and (3) perform the optimization and sample posterior distributions via MCMC methods. Many attributes (such as initial parameters) are shared in multiple layers of this hierarchy for easier access and extension with appropriate methods to propagate changes to each. `Optimize` does not reimplement specific optimization algorithms, but rather is intended to be a high-level wrapper around such routines (e.g., currently `scipy.optimize` and `emcee`).

Appendix C

RV Measurements

Table 7

BJD	RV (m s ⁻¹)	σ_{RV} (m s ⁻¹)
Nightly HARPS RVs Analyzed in This Work		
2452986.514817	73.91	4.81
2453157.898424	19.26	1.72
2453201.823450	-32.8	2.56
2453468.892370	-135.2	2.52
2453469.843534	-170.56	2.92
2453499.868255	-43.41	2.52
2453521.894368	-345.97	6.36
2453551.803998	-34.22	2.5
2453593.622139	137.84	3.33
2456568.510365	-244.53	2.16
2456569.500104	-32.99	1.8
2456570.565952	193.28	2.17
2456772.919271	-54.34	1.64
2456773.918979	-9.22	0.99
2456794.882288	-119.81	2.53
2456795.885873	66.36	2.91
2456797.857541	20.03	3.0
2456844.806163	162.85	2.18
2456982.539577	-65.03	1.8
2457223.648073	217.24	2.71
2457333.535731	94.85	1.29
2457493.891905	90.65	2.11
2457590.712986	73.08	1.4
2457904.813342	-287.06	3.36
2457917.892902	161.13	1.97
2458035.528955	-22.13	1.55
2458037.494745	-41.59	2.39
2458206.872213	-43.23	1.38
2458207.892023	33.78	1.56
2458208.884974	82.61	1.29
2458591.919473	120.82	1.42
2458594.904828	19.89	2.43
2458602.927758	9.22	1.47
2458605.916360	-248.46	2.33
Nightly HIRES RVs Analyzed in This Work		
2453182.049556	58.09	4.01
2453195.938633	-171.02	2.74

Table 7
(Continued)

BJD	RV (m s ⁻¹)	σ_{RV} (m s ⁻¹)
2453926.030459	-270.15	3.02
2453926.979641	271.86	3.18
2453927.920257	68.35	2.13
2453931.079663	-191.25	3.16
2453932.007322	256.77	2.76
2453932.978973	7.97	2.18
2453933.944291	162.29	2.36
2453934.930418	-159.79	2.73
2453960.942379	257.92	2.98
2453962.030949	5.08	2.28
2454636.072465	-9.82	2.53
2454688.871239	-133.07	2.46
2454808.692607	-83.96	3.06
2455015.018198	-140.72	2.86
2455371.044475	100.3	1.9
2455727.981919	35.73	2.89
2456638.683238	325.16	4.18
2458645.065398	-77.3	7.43
2459019.062251	-121.05	2.81
2459025.094631	-155.66	2.48
2459026.123675	399.32	3.35
2459028.098307	104.1	2.86
2459029.081905	14.31	2.53
2459030.078281	-131.6	2.19
2459031.106844	414.91	3.41
2459032.105577	-138.95	2.71
2459035.092001	-76.31	2.26
2459036.101597	329.39	3.4
2459040.116030	3.72	2.12
2459041.117761	153.21	3.14
2459044.942379	-0.97	2.22
2459051.921900	92.94	2.44
2459067.855784	-21.57	3.09
2459068.895396	-30.19	2.4
2459071.907618	43.81	3.37
2459072.852897	-8.9	2.74
2459077.821906	-44.12	2.71
2459078.813958	-31.15	2.45
2459086.849156	-147.83	3.51
2459087.868995	0.97	2.58
2459088.849805	139.3	2.57
2459089.824376	-38.53	3.28
2459094.815792	-127.27	2.67
2459097.855698	-16.26	2.6
2459099.761856	-139.97	3.05
2459101.904682	-82.58	2.51
2459114.829534	-6.09	2.08
2459115.914980	-92.15	2.61
2459117.857924	48.2	2.29
2459121.710044	11.92	2.38
2459122.709275	58.74	2.34
2459123.703587	20.0	2.6
2459151.692854	40.18	2.41
2459153.753326	95.26	2.73
2459181.680326	42.79	2.6
2459187.682871	54.26	2.47
2459188.689611	-6.89	2.6
2459189.684349	-81.15	2.86
Nightly NIRSPEC RVs Analyzed in This Work		
2453522.56	48.5	50.0
2453523.55	-19.5	50.0
2453596.37	111.5	50.0
2453597.38	19.5	50.0

⁵⁶ Documentation: <https://optimize.readthedocs.io/en/latest/>.

Table 7
(Continued)

BJD	RV (m s^{-1})	σ_{RV} (m s^{-1})
2453669.19	113.5	50.0
2453670.2	262.5	50.0
2453928.5	-74.5	50.0
2453929.45	-148.5	50.0
2453930.46	-93.5	50.0
2453931.4	-24.5	50.0
2454308.43	123.5	50.0
2454309.41	-166.5	50.0
2454311.4	20.5	50.0
2454312.36	-157.5	50.0
Nightly CSHELL RVs Analyzed in This Work		
2455455.85303	16.79	38.76
2455479.800206	41.04	26.96
2455480.768983	143.4	56.64
2455482.756068	136.64	22.11
2455523.7002290003	0.0	20.78
2455752.0995830004	43.59	27.48
2455755.0752310003	141.67	44.57
2455758.967657	-17.29	31.52
2455791.812748	123.61	54.8
2455793.8316450003	234.74	10.87
2456844.9609169997	-35.3	15.47
2456917.743247	-36.65	21.07
2457275.8463990004	-115.88	26.14
2457551.12512	-102.38	51.72
2457555.058318	-150.06	20.78
2457564.0072459998	-198.34	30.4
2457570.063826	82.72	36.9
2457587.023049	-245.01	18.85
2457598.976608	-90.04	25.01
2457618.963993	8.92	19.22
2457619.947171	-72.55	21.1
Nightly TRES RVs Analyzed in This Work		
2456573.68979	-128.0	11.6
2456574.640606	-45.2	11.8
2456575.669816	183.9	14.4
2456576.660338	-186.6	10.3
2456577.632961	203.9	12.3
2456578.625675	-68.1	11.9
2456579.634451	-64.0	13.8
2456580.634669	173.3	13.7
2456581.610641	-117.8	11.3
2456582.623658	101.1	21.4
2456583.619796	-35.2	9.7
2456584.624069	-18.7	11.0
2456585.596255	59.0	11.7
2456586.617077	-22.2	12.7
2456587.611581	0.0	11.7
2456588.591012	-33.7	11.6
2456589.602899	45.0	11.8
2456590.622533	-64.4	12.1
2456605.581655	-250.0	13.7
2456606.565507	225.6	8.4
2456607.563214	-172.0	12.1
2456608.58807	-11.5	10.6
2456609.587085	211.2	13.7
2456610.565465	-233.4	15.0
2456611.571286	213.0	9.2
2456615.560722	-193.0	13.6
2456616.572477	176.9	13.8
2456622.557557	-102.5	19.3
2456624.552961	85.6	46.8

Table 7
(Continued)

BJD	RV (m s^{-1})	σ_{RV} (m s^{-1})
2456625.563003	38.7	24.7
2458646.96613	49.9	24.2
2458647.964611	34.3	22.0
2458648.961007	-44.6	17.8
2458649.958409	-41.2	18.9
2458650.97301	164.3	16.2
2458651.966405	116.1	17.5
2458652.981466	-33.8	24.0
2458657.953559	13.6	15.7
2458658.932441	-107.5	17.0
2458659.912405	84.9	19.9
2458665.924079	130.6	17.8
2458674.932143	198.8	14.2
2458677.882169	-99.1	20.1
2458685.884899	96.1	35.5
2458689.846153	110.1	14.7
2458693.842764	-74.1	24.1
2458730.740018	17.1	23.4
2458731.739653	-35.0	23.9
2458738.70382	145.2	32.6
2458742.696035	-86.4	40.1
2458744.700854	234.4	25.3
2458745.730511	-65.9	40.3
2458758.650170	42.1	25.3
2458759.694882	114.5	28.3
2458761.645681	-117.3	17.2
2458762.677499	144.6	21.8
2458767.656488	107.5	33.1
2458768.653311	83.7	30.6
2458769.635106	15.1	22.5
2458770.623329	-112.3	18.2
2458771.612582	-144.9	21.1
2458772.628816	120.2	22.4
2458773.638865	91.1	25.1
2458774.591042	-51.3	25.3
2458775.598544	-135.9	24.1
2458779.573710	-86.3	24.1
2458780.566456	-148.0	20.2
2458782.572973	29.7	19.0
2458783.561459	123.9	30.0
2458784.56098	-121.1	21.7
2458786.591881	-45.4	22.6
2458787.627174	-2.0	29.9
2458788.570062	211.2	22.7
Nightly iSHELL RVs Analyzed in This Work		
2457684.759584	76.97	4.94
2457698.745971	47.96	3.05
2457699.710324	47.8	14.07
2457850.129559	87.59	7.24
2457856.130267	-33.33	3.41
2457923.120317	-1.31	4.77
2457931.026094	-15.53	1.59
2457940.000525	-7.44	0.26
2457982.918015	-2.11	11.34
2457983.911491	-25.53	31.67
2457984.906727	76.12	7.17
2458046.688896	-53.89	6.97
2458047.677782	20.45	9.09
2458048.684528	1.5	7.03
2458049.677166	-68.12	11.49
2458660.089282	8.42	3.31
2458666.92506	42.5	2.21
2458675.084455	71.1	4.86

Table 7
(Continued)

BJD	RV (m s ⁻¹)	σ_{RV} (m s ⁻¹)
2458739.930751	85.7	4.12
2458760.71097	-48.38	4.51
2458761.729422	-96.54	3.37
2458762.730214	16.08	6.35
2458763.779074	-14.43	3.17
2458764.766543	18.96	5.06
2458765.711105	-39.79	7.94
2458795.700288	-59.42	3.14
2458796.706964	-0.86	5.37
2458798.695629	32.0	4.13
2458799.69492	-22.28	9.62
2459069.985765	67.29	11.02
2459071.979622	24.53	3.5
2459086.915335	-5.96	4.43
2459087.917716	68.09	13.17
2459088.900423	39.07	5.6
2459089.900047	20.73	7.19
2459090.897927	50.16	4.41
2459115.810803	-7.73	5.78
2459117.805977	-23.08	3.53
2459118.807183	-12.72	4.15
2459119.813063	3.98	5.34
2459120.804824	-28.18	4.32
2459122.88224	3.77	4.62
2459123.807924	-16.94	5.09
2459143.789273	-35.3	5.73
2459145.789894	0.86	9.38
2459147.782831	-7.73	4.04
Nightly IRD RVs Analyzed in This Work		
2458650.116682	-36.37	2.06
2458653.123778	5.82	4.63
2458654.116977	-62.9	1.88
2458655.126277	42.79	1.75
2458679.945743	1.82	5.4
2458771.845784	-1.82	3.99

Nightly CARMENES-NIR RVs Analyzed in This Work

2458678.567915	92.38	46.13
2458679.537705	315.17	54.39
2458680.53478	247.69	65.59
2458684.568375	437.36	75.05
2458686.548525	275.14	49.79
2458687.578395	201.29	45.37
2458688.584370	86.47	46.79
2458690.55771	180.81	23.17
2458691.505425	276.31	30.81
2458693.54918	-19.49	18.84
2458694.59554	164.36	19.65
2458695.53909	-3.88	25.06
2458696.523080	41.45	15.91
2458698.51838	-112.18	13.87
2458699.48421	43.11	18.82
2458700.47701	-12.46	23.43
2458701.471955	-38.69	30.48
2458702.50203	-267.32	55.65
2458704.48929	-7.34	25.96
2458706.498265	-60.66	24.28
2458711.444815	-64.13	25.69
2458712.45243	-208.9	30.92
2458714.507735	-1.04	29.74
2458715.454715	104.33	19.43
2458718.45001	10.36	23.92
2458723.46396	-10.17	29.09

Table 7
(Continued)

BJD	RV (m s ⁻¹)	σ_{RV} (m s ⁻¹)
2458724.419910	-4.56	29.82
2458727.47503	-162.58	33.76
2458742.39457	-78.27	23.94
2458743.368875	105.08	32.28
2458744.35226	96.0	17.59
2458745.395085	-0.64	29.71
2458755.39838	-10.29	41.43
2458757.375210	-54.66	41.67
2458759.369515	121.73	27.43
2458760.30872	10.36	28.45
2458761.35095	-120.87	25.35
2458763.336130	26.53	27.49
2458765.32907	-24.44	46.17
2458766.329605	-141.11	33.1
2459049.54651	177.28	83.51
2459050.5627	326.43	75.53
2459051.54861	164.54	58.18
2459059.517	128.17	38.35
2459060.56397	0.64	45.11
2459061.51774	-1.64	26.11
2459067.51658	-22.7	35.8
2459070.49213	-161.95	47.51
2459076.47969	53.98	28.45
2459078.48314	-53.38	47.45
2459079.51194	84.71	32.93
2459081.44324	-7.63	44.14
2459085.4860900003	-66.12	30.86
2459086.47407	-5.4	35.27
2459087.44822	43.18	42.15
2459095.462660	13.58	28.27
2459098.44795	15.8	34.37
2459099.41347	0.86	35.8
2459148.30047	-76.46	68.62
2459154.2969	25.34	66.01
2459161.27302	-70.52	61.17
2459170.25901	-35.74	60.54

Nightly CARMENES-VIS RVs Analyzed in This Work

2458678.568125	-69.66	29.45
2458679.537290	241.65	40.59
2458680.53527	79.92	15.96
2458684.568335	232.51	25.58
2458686.54842	177.2	16.04
2458687.578910	-17.01	20.79
2458688.584365	-96.42	19.21
2458690.5572350	114.83	11.18
2458691.505425	155.65	13.93
2458693.549395	-100.78	8.52
2458694.59568	135.7	6.79
2458695.53932	39.93	10.69
2458696.522970	57.79	6.7
2458698.518795	-108.57	4.86
2458699.484225	81.68	8.55
2458700.47709	10.01	6.31
2458701.472325	-1.34	7.9
2458702.502	-163.13	16.45
2458704.489635	79.4	7.75
2458706.498955	-53.41	13.14
2458711.445175	-68.26	9.3
2458712.452575	-145.53	8.27
2458714.507445	74.89	11.13
2458715.454290	119.79	6.96
2458718.449865	-8.15	7.88
2458723.46386	10.82	9.14

Table 7
(Continued)

BJD	RV (m s ⁻¹)	σ_{RV} (m s ⁻¹)
2458724.42014	32.17	9.24
2458727.47467	-120.64	15.58
2458742.394525	-111.51	6.47
2458743.36923	109.79	10.05
2458744.35274	44.66	6.63
2458745.394785	-8.64	10.77
2458755.399070	-52.31	12.96
2458757.37524	-40.49	11.8
2458759.369535	173.63	10.1
2458760.30896	-50.26	9.67
2458761.350815	-127.71	8.52
2458763.33635	21.39	6.78
2458765.32879	-83.71	9.85
2458766.32998	-150.2	7.98
2459049.54617	-9.06	23.94
2459050.56301	261.02	21.89
2459051.54856	-21.26	27.7
2459059.51739	21.86	12.02
2459060.56385	56.21	15.25
2459061.51767	3.43	9.96
2459067.51635	-61.79	14.71
2459070.49224	-120.99	17.32
2459076.47973	74.87	9.62
2459078.48285	-66.09	12.86
2459079.51202	159.74	17.82
2459081.4433	18.72	16.94
2459085.48611	-103.96	11.19
2459086.47053	0.0	11.41
2459087.44817	-22.76	10.14
2459095.46273	-17.99	15.28
2459098.44771	36.94	14.87
2459099.41364	1.26	13.44
2459113.41579	77.58	40.76
2459148.3007	-199.06	41.82
2459154.29727	80.14	23.03
2459161.27325	-25.96	17.31
2459170.25874	-52.59	15.02
Nightly MINERVA-Australis RVs Analyzed in This Work		
2458683.150648	89.06	38.22
2458684.165833	208.9	10.54
2458711.967436	-67.42	12.5
2458716.998287	-61.47	10.95
2458719.003218	175.13	22.44
2458720.062263	81.08	6.24
2458725.959649	32.34	104.73
2458738.040897	-55.32	7.36
2458739.963764	235.89	6.39

Table 7
(Continued)

BJD	RV (m s ⁻¹)	σ_{RV} (m s ⁻¹)
2458740.989093	-125.63	5.43
2458741.999722	-128.95	8.06
2458743.006845	0.0	5.15
2458792.965243	-13.18	9.52
Nightly CHIRON RVs Analyzed in This Work		
2458740.72096	1.48	45.24
2458741.713716	149.09	46.54
2458742.711554	-54.11	37.64
2458762.643643	112.47	56.45
2458763.64337	-44.57	36.34
2458764.629147	72.97	42.89
2458765.631185	-310.79	58.25
2458766.614416	-169.88	44.79
2458795.574927	51.27	68.8
2458796.570968	-1.48	71.87
2458797.56992	-11.17	37.07
2458798.597397	359.32	52.94
Nightly SPIRou RVs Analyzed in This Work		
2458744.8212	59.5	5.0
2458750.7542	-18.2	5.0
2458751.7453	-52.4	5.0
2458752.7898	27.9	5.0
2458758.7288	51.3	5.0
2458759.8053	69.2	5.0
2458760.7278	-29.6	5.0
2458761.7305	-87.2	5.0
2458762.7315	-2.9	5.0
2458764.7571	34.5	5.0
2458765.7694	-39.8	5.0
2458769.7438	22.1	5.0
2458770.7407	-41.6	5.0
2458771.7212	-55.8	5.0
2458772.7416	19.4	5.0
2458787.7155	28.3	5.0
2458788.7045	41.3	5.0
2458789.7367	-32.6	5.0
2458790.701	-90.1	5.0
2458791.6983	2.1	5.0
2458792.6976	19.1	5.0
2458796.6859	-13.5	5.0
2458797.7098	19.7	5.0
2458798.6873	27.0	5.0
2458799.6883	-10.3	5.0
2458800.6896	-46.2	5.0
2458801.6873	0.0	5.0

Appendix D Fitting the Full RV Data Set

Here, we present fits to the full radial-velocity data set (see Section 2). Although the baseline of the full data set is nearly 17 yr (first epoch in 2003 December), the uncertainties for the

period and time of transit for AU Mic b and c are small enough to be fixed (see Table 2). We only use kernel K_{J2} (Equation (3)) to model the stellar activity, as we do not seek to fit for per-spectrograph activity amplitudes for data sets with $\lesssim 10$ measurements. A first-order estimation for the secular acceleration (Choi et al. 2013) of AU Mic is negligible,

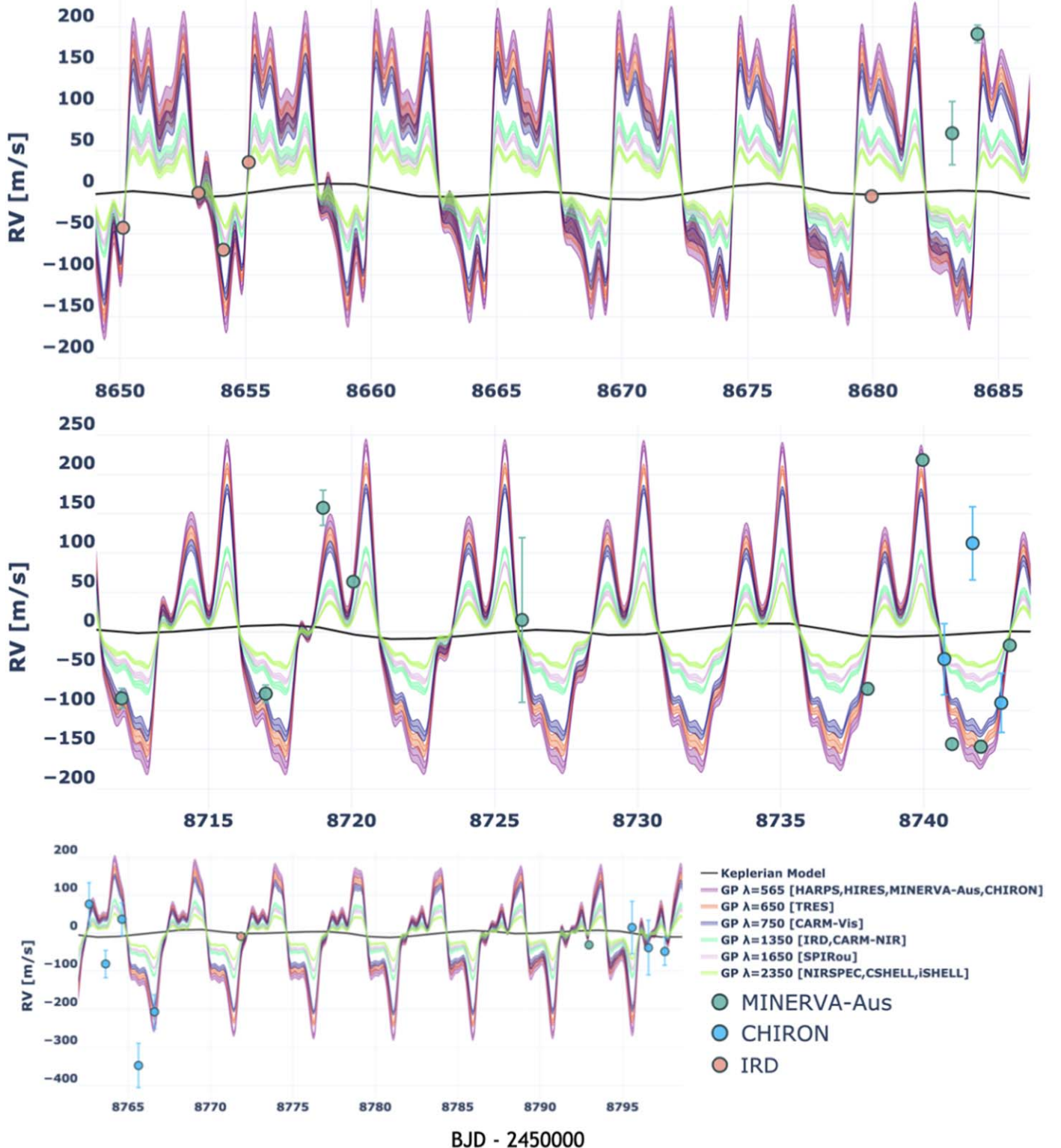


Figure 19. Here, we show a subset of the 2019 RVs using kernel K_{J2} (Equation (2)) to model the stellar activity and including the full RV data set. Although we do not include the MINERVA-Australis or IRD RVs in our primary fits in Section 3, we find they are generally consistent with our stellar activity model. We do not show the phased CHIRON RVs, due to their larger residuals.

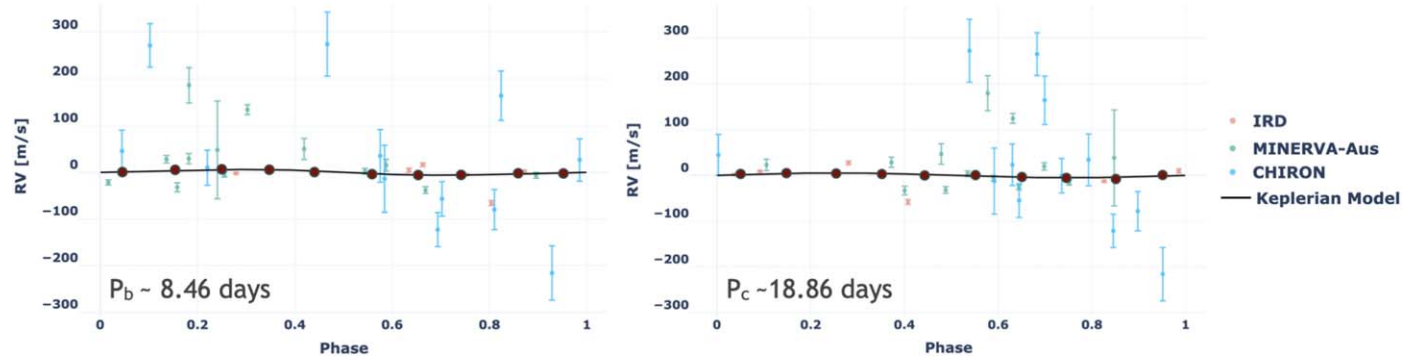


Figure 20. Same as Figure 19, but showing the phased RVs.

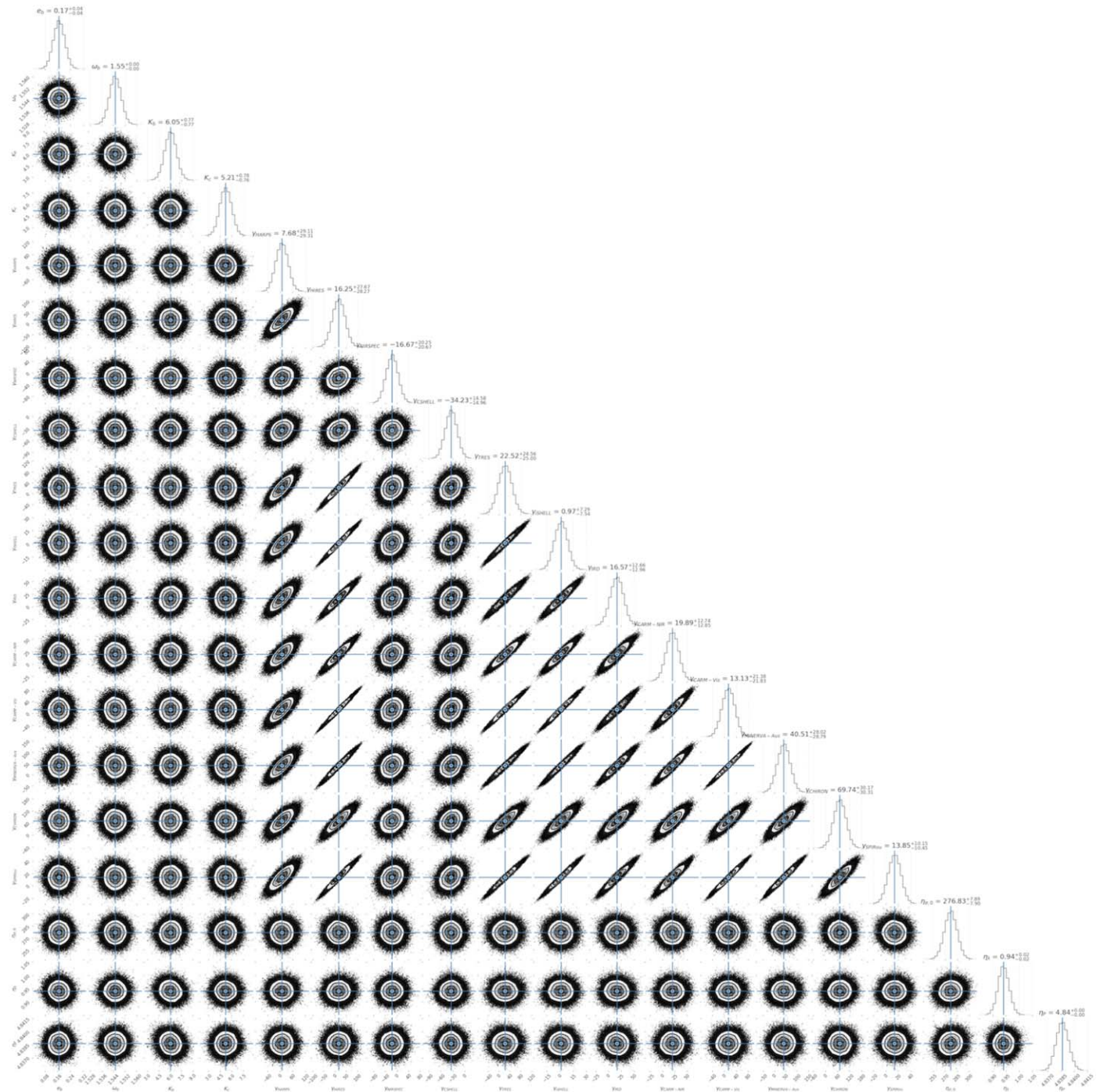


Figure 21. Posterior distributions for a two-planet fit to the full RV data set using K_{J2} to model the stellar activity. Blue lines correspond to the 50th percentile of the distribution. Upper and lower uncertainties correspond to the 15.9th and 84.1st percentiles, respectively. The semi-amplitude K_b is $\approx 30\%$ smaller than the subset of 2019–2020 data yields (Table 3), but K_c is relatively unchanged.

given the precision of our measurements and baseline ($\Delta RV < 3 \text{ cm s}^{-1}$), so no long-term linear or quadratic trend is used. The GPs and Keplerian model are shown in Figure 19, and the phased RVs are shown in Figure 20. The posteriors are shown in Figure 21.

ORCID iDs

- Bryson L. Cale  <https://orcid.org/0000-0001-6279-0595>
Peter Plavchan  <https://orcid.org/0000-0002-8864-1667>
Eric Gaidos  <https://orcid.org/0000-0002-5258-6846>
Jonathan Gagné  <https://orcid.org/0000-0002-2592-9612>

- Peter Gao  <https://orcid.org/0000-0002-8518-9601>
Stephen R. Kane  <https://orcid.org/0000-0002-7084-0529>
Víctor J. S. Béjar  <https://orcid.org/0000-0002-5086-4232>
Nicolas Lodieu  <https://orcid.org/0000-0002-3612-8968>
Ignasi Ribas  <https://orcid.org/0000-0002-6689-0312>
Enric Pallé  <https://orcid.org/0000-0003-0987-1593>
Andrew W. Howard  <https://orcid.org/0000-0001-8638-0320>
Benjamin J. Fulton  <https://orcid.org/0000-0003-3504-5316>
Kevin I. Collins  <https://orcid.org/0000-0003-2781-3207>
Justin Wittrock  <https://orcid.org/0000-0002-7424-9891>
Emily A. Gilbert  <https://orcid.org/0000-0002-0388-8004>

Thomas Barclay [DOI](https://orcid.org/0000-0001-7139-2724)
 Robert Wittenmyer [DOI](https://orcid.org/0000-0001-9957-9304)
 Duncan Wright [DOI](https://orcid.org/0000-0001-7294-5386)
 Brett Addison [DOI](https://orcid.org/0000-0003-3216-0626)
 Teruyuki Hirano [DOI](https://orcid.org/0000-0003-3618-7535)
 Motohide Tamura [DOI](https://orcid.org/0000-0002-6510-0681)
 Norio Narita [DOI](https://orcid.org/0000-0001-8511-2981)
 Samuel N. Quinn [DOI](https://orcid.org/0000-0002-8964-8377)
 David W. Latham [DOI](https://orcid.org/0000-0001-9911-7388)
 Gilbert A. Esquerdo [DOI](https://orcid.org/0000-0002-9789-5474)
 Michael L. Calkins [DOI](https://orcid.org/0000-0002-2830-5661)
 Jon Jenkins [DOI](https://orcid.org/0000-0002-4715-9460)
 Joseph D. Twicken [DOI](https://orcid.org/0000-0002-6778-7552)
 Christopher Burke [DOI](https://orcid.org/0000-0002-7754-9486)
 Patricia Boyd [DOI](https://orcid.org/0000-0003-0442-4284)

References

- Addison, B., Wright, D. J., Wittenmyer, R. A., et al. 2019, *PASP*, **131**, 115003
 Addison, B. C., Wright, D. J., Nicholson, B. A., et al. 2021, *MNRAS*, **502**, 3704
 Aigrain, S., Pont, F., & Zucker, S. 2012, *MNRAS*, **419**, 3147
 Akaike, H. 1974, *ITAC*, **19**, 716
 Allard, F., Homeier, D., & Freytag, B. 2012, *RSPTA*, **370**, 2765
 Anglada-Escudé, G., & Butler, R. P. 2012, *ApJS*, **200**, 15
 Bailey, J. I., White, R. J., Blake, C. H., et al. 2012, *ApJ*, **749**, 16
 Barnes, S. I., Gibson, S., Nield, K., & Cochrane, D. 2012, *Proc. SPIE*, **8446**, 844688
 Batalha, N. E., Lewis, T., Fortney, J. J., et al. 2019, *ApJL*, **885**, L25
 Bauer, F. F., Zechmeister, M., Kaminski, A., et al. 2020, *A&A*, **640**, A50
 Buchhave, L. A., Bakos, G. Á., Hartman, J. D., et al. 2010, *ApJ*, **720**, 1118
 Burnham, K. P., & Anderson, D. R. 2002, Model Selection and Multimodel Inference (Berlin: Springer)
 Caballero, J. A., Guàrdia, J., López del Fresno, M., et al. 2016, *Proc. SPIE*, **9910**, 99100E
 Cale, B., Plavchan, P., LeBrun, D., et al. 2019, *AJ*, **158**, 170
 Chen, J., & Kipping, D. 2017, *ApJ*, **834**, 17
 Choi, J., McCarthy, C., Marcy, G. W., et al. 2013, *ApJ*, **764**, 131
 Cretignier, M., Dumusque, X., Allart, R., Pepe, F., & Lovis, C. 2020, *A&A*, **633**, A76
 Czesla, S., Schröter, S., Schneider, C. P., et al. 2019, PyA: Python Astronomy-related Packages, Astrophysics Source Code Library, ascl:[1906.010](https://ascl.net/1906.010)
 Desort, M., Lagrange, A. M., Galland, F., Udry, S., & Mayor, M. 2007, *A&A*, **473**, 983
 Donati, J.-F., Kouach, D., Lacombe, M., et al. 2018, in SPIRou: A NIR Spectropolarimeter/High-Precision Velocimeter for the CFHT, ed. H. J. Deeg & J. A. Belmonte (Berlin: Springer), 107
 Dumusque, X. 2018, *A&A*, **620**, A47
 Dumusque, X., Boisse, I., & Santos, N. C. 2014, *ApJ*, **796**, 132
 Foreman-Mackey, D., Hogg, D. W., Lang, D., & Goodman, J. 2013, *PASP*, **125**, 306
 Foreman-Mackey, D., Price-Whelan, A., Vounoudzou, W., et al. 2020, dfm/corner.py: corner.py v2.1.0.rc1, v2.1.0.rc1, Zenodo, doi:[10.5281/zenodo.3937526](https://doi.org/10.5281/zenodo.3937526)
 Fulton, B. J., Petigura, E. A., Blunt, S., & Sinukoff, E. 2018, *PASP*, **130**, 044504
 Fűrész, G. 2008, PhD thesis, University of Szeged, Hungary, <http://www.sao.arizona.edu/html/FLWO/60/TRES/GABORthesis.pdf>
 Gaia Collaboration, Brown, A. G. A., Vallenari, A., et al. 2018, *A&A*, **616**, A1
 Gagné, J., Plavchan, P., Gao, P., et al. 2016, *ApJ*, **822**, 40
 Gao, P., Plavchan, P., Gagné, J., et al. 2016, *PASP*, **128**, 104501
 Gilbert, E. A., Barclay, T., & Quintana, E. V. 2021, arXiv:[2109.03924](https://arxiv.org/abs/2109.03924)
 Greene, T. P., Tokunaga, A. T., Toomey, D. W., & Carr, J. B. 1993, *Proc. SPIE*, **1946**, 313
 Grunblatt, S. K., Howard, A. W., & Haywood, R. D. 2015, *ApJ*, **808**, 127
 Harris, C. R., Millman, K. J., van der Walt, S. J., et al. 2020, *Natur*, **585**, 357
 Haywood, R. D. 2015, PhD thesis, University of St. Andrews
 Haywood, R. D., Collier Cameron, A., Queloz, D., et al. 2014, *MNRAS*, **443**, 2517
 Hirano, T., Krishnamurthy, V., Gaidos, E., et al. 2020a, *ApJL*, **899**, L13
 Hirano, T., Kuzuhara, M., Kotani, T., et al. 2020b, *PASJ*, **72**, 93
 Howard, A. W., Johnson, J. A., Marcy, G. W., et al. 2010, *ApJ*, **721**, 1467
 Hunter, J. D. 2007, *CSE*, **9**, 90
 Inc., P. T. 2015, Collaborative Data Science (Montreal, QC: Plotly Technologies Inc.), <https://plot.ly>
 Jeffreys, H. 1946, *RSPSA*, **186**, 453
 Jenkins, J. M., Twicken, J. D., McCauliff, S., et al. 2016, *Proc. SPIE*, **9913**, 99133E
 Jones, E., Oliphant, T., Peterson, P., et al. 2001, SciPy: Open Source Scientific Tools for Python, <http://www.scipy.org/>
 Klein, B., Donati, J.-F., Moutou, C., et al. 2021, *MNRAS*, **502**, 188
 Kotani, T., Tamura, M., Nishikawa, J., et al. 2018, *Proc. SPIE*, **10702**, 1070211
 Lam, S. K., Pitrou, A., & Seibert, S. 2015, Numba: A LLVM-based Python jit Compiler
 Lo Curto, G., Beniflah, T., Burrows, A., et al. 2010, *Msngr*, **142**, 42
 López-Morales, M., Haywood, R. D., Coughlin, J. L., et al. 2016, *AJ*, **152**, 204
 Mamajek, E. E., & Bell, C. P. M. 2014, *MNRAS*, **445**, 2169
 Martioli, E., Hébrard, G., Correia, A. C. M., Laskar, J., & Lecavelier des Etangs, A. 2021, *A&A*, **649**, A177
 Mayor, M., Pepe, F., Queloz, D., et al. 2003, *Msngr*, **114**, 20
 McLean, I. S., Becklin, E. E., Bendiksen, O., et al. 1998, *Proc. SPIE*, **3354**, 566
 Meunier, N., & Lagrange, A. M. 2013, *A&A*, **551**, A101
 NASA Exoplanet Archive 2019, Confirmed Planets Table, IPAC, doi:[10.26133/NEA1](https://doi.org/10.26133/NEA1)
 Pecaut, M. J., & Mamajek, E. E. 2013, *ApJS*, **208**, 9
 Piskunov, N. E., & Valenti, J. A. 2002, *A&A*, **385**, 1095
 Plavchan, P., Barclay, T., Gagné, J., et al. 2020, *Natur*, **582**, 497
 Quinn, S. N., White, R. J., Latham, D. W., et al. 2014, *ApJ*, **787**, 27
 Quirrenbach, A., Amado, P. J., Ribas, I., et al. 2018, *Proc. SPIE*, **10702**, 107020W
 Rajpaul, V., Aigrain, S., Osborne, M. A., Reece, S., & Roberts, S. 2015, *MNRAS*, **452**, 2269
 Rasmussen, C. E., & Williams, C. K. I. 2006, Gaussian Processes for Machine Learning (Berlin: Springer)
 Rayner, J., Tokunaga, A., Jaffe, D., et al. 2016, *Proc. SPIE*, **9908**, 990884
 Reiners, A., Bean, J. L., Huber, K. F., et al. 2010, *ApJ*, **710**, 432
 Reiners, A., & Zechmeister, M. 2020, *ApJS*, **247**, 11
 Ricker, G. R., Winn, J. N., Vanderspek, R., et al. 2015, *JATIS*, **1**, 014003
 Robertson, P., Stefansson, G., Mahadevan, S., et al. 2020, *ApJ*, **897**, 125
 Smith, J. C., Stumpe, M. C., Van Cleve, J. E., et al. 2012, *PASP*, **124**, 1000
 Stumpe, M. C., Smith, J. C., Catanzarite, J. H., et al. 2014, *PASP*, **126**, 100
 Stumpe, M. C., Smith, J. C., Van Cleve, J. E., et al. 2012, *PASP*, **124**, 985
 Swade, D., Fleming, S., Jenkins, J. M., et al. 2018, *Proc. SPIE*, **10704**, 1070415
 Szabó, G. M., Gandolfi, D., Brandeker, A., et al. 2021, *A&A*, **654**, A159
 Tody, D. 1993, in ASP Conf. Ser. 52, Astronomical Data Analysis Software and Systems II, ed. R. J. Hanisch, R. J. V. Brissenden, & J. Barnes (San Francisco, CA: ASP), 173
 Tokovinin, A., Fischer, D. A., Bonati, M., et al. 2013, *PASP*, **125**, 1336
 Toledo-Padrón, B., Suárez Mascareño, A., González Hernández, J. I., et al. 2021, *A&A*, **648**, A20
 Trifonov, T., Kürster, M., Zechmeister, M., et al. 2018, *A&A*, **609**, A117
 Tronskaagard, R., Buchhave, L. A., Wright, J. T., Eastman, J. D., & Blackman, R. T. 2019, *MNRAS*, **489**, 2395
 Virtanen, P., Gommers, R., Oliphant, T. E., et al. 2020, *NatMe*, **17**, 261
 Vogt, S. S., Allen, S. L., Bigelow, B. C., et al. 1994, *Proc. SPIE*, **2198**, 362
 Wise, A. W., Dodson-Robinson, S. E., Bevenour, K., & Provini, A. 2018, *AJ*, **156**, 180
 Wittenmyer, R. A., Horner, J., Carter, B. D., et al. 2018, arXiv:[1806.09282](https://arxiv.org/abs/1806.09282)
 Zechmeister, M., & Kürster, M. 2018, GLS: Generalized Lomb-Scargle Periodogram, Astrophysics Source Code Library, ascl:[1807.019](https://ascl.net/1807.019)
 Zechmeister, M., Reiners, A., Amado, P. J., et al. 2018, *A&A*, **609**, A12